IMPROVEMENT OF TIME-OF-FLIGHT SPECTROMETER
FOR ELASTIC RECOIL DETECTION ANALYSIS

BY

MIKKO LAITINEN

Academic Dissertation
for the Degree of
Doctor of Philosophy

To be presented, by the permission of the
Faculty of Mathematics and Natural Sciences
for the University of Jyväskylä
for public examination in Auditorium FYS1 of the
University of Jyväskylä on December 20th, 2013
at 12 o'clock noon

Jyväskylä, Finland
December 2013

Preface

This work reported in this thesis has been carried out during 2005-2013 at the Department of Physics, University of Jyväskylä. These years, during which our research group has significantly changed size, persons, research direction and tools, have been very valuable for a PhD student like me in many respects.

I have been able both to impact the decisions and asses the consequences for the changes mentioned above. This has integrated me more deeply to the world of research and also to the education through the Department of Physics. There were also periods when it seemed that I was helping more others than was devoting time to "my own" work. However, I have valued all the experiences from these efforts high as long as I have also learnt something new from these different tasks. Being able to take part so many different projects, I have also gained many friends who have helped me and for whom I now want to express my thanks.

Timo, I was among the persons who decided to hire you to the Department. That was not a bad choice. You on the other hand was taking me under your wings at 2005 when I started working as a PhD student. The group, without the accelerator of its own, was an accelerator based materials research group, whom you now have become a distinguished leader of. In early years, with your personal contacts, the group received its primary research tool, the accelerator, similarly as I took equally part building it together and keeping it running with you. Without your vision this group would not have flourished as it is now. This same sentence applies also to me. For your guidance, comments and other discussions, thank you.

Then there is a list of many. Sergey, Ananda, Somjai, Book, Liping, Jiku, to mention few not that native when they arrived but you had become more native than many Finns, when you left from our group. With you it really was a pleasure to work with and even more: to actually know you, thanks! You are the ones I miss the most in our research group.

Laura, Jaakko, Mari, the other PhD students of our current group, from you I have always received help when needed. Useful comments and even counterarguments, mostly from Jaakko, have been always welcomed. Kai, always willing to help and Jari, now the ALD specialist of the group, it is certain that with your valuable effort the group will rise to the new level in the near future. For me, Antti, the long-time roommate in the FL127, you were always something that I could count on. I thank all of you equally.

My family and the beloved ones at home, Katri and Aada, without your warmth and presence at home I would not be complete, neither at work or at home. You have been my strength and support. I love you.

Jyväskylä 1.12.2013

Mikko Laitinen

Abstract

Laitinen, Mikko
Improvement of time-of-flight spectrometer for elastic recoil detection analysis
Jyväskylä, University of Jyväskylä, 2013, 71 p.
Department of Physics Research Report No. 12/2013
ISBN paper copy: 978-951-39-5546-5
ISBN PDF: 978-951-39-5547-2
ISSN: 0075-465X

Quantitative elemental analysis of thin film samples has been possible in Jyväskylä since 2007 by means of Rutherford backscattering spectrometry. Depth profiling of all elements, including hydrogen, became possible in 2009 after the Time-of-Flight–Elastic Recoil Detection Analysis spectrometer was built. This spectrometer is characterized in this thesis. Since then this tool has been used for characterization of all sample elements from hundreds of samples. Some more exotic samples include Al_2O_3/TiO_2 nanolaminates and sub-monolayer thick atomic layer deposited Al_2O_3 films on top of TiO_2 which are included in this work as examples. This thesis is focused on the understanding of two timing detectors as a part of a timing telescope of the ToF-ERDA spectrometer. With the help of experimental measurements together with the simulations, an explanation for the origin of the halo structure around the light elements in the ToF-E histograms is given. Also the so called tandem effect which limits the energy resolution of the carbon foil time pick-up detectors and the bending of the low energy protons in the electric fields of the detectors were simulated in detail.

Keywords: Time of flight elastic recoil detection analysis, ToF-ERDA, time-of-flight, ToF, timing gate, elemental depth profiling

Author   Mikko Laitinen
                  Department of Physics
                  University of Jyväskylä
                  P.O. Box 35
                  40014 Finland
                  mikko.i.laitinen@jyu.fi

Supervisor   Dr. Timo Sajavaara
                  Department of Physics
                  University of Jyväskylä
                  P.O. Box 35
                  40014 Finland
                  timo.sajavaara@jyu.fi

Reviewers   Dr. Pertti O. Tikkanen,
                  University of Helsinki, Finland
                  pertti.tikkanen@helsinki.fi

                  Dr. Jens Jensen,
                  Linköping University, Sweden
                  jejen@ifm.liu.se

Opponent   Dr. Ivančica Bogdanović-Radović,
                  Ruđer Bošković Institut, Croatia
                  iva@irb.hr

List of Publications

[I]   Time-of-flight – energy spectrometer for elemental depth profiling - Jyväskylä design;

Mikko Laitinen, Mikko Rossi, Jaakko Julin and Timo Sajavaara

Submitted to: Nucl. Instr. and Meth. A

[II] Secondary electron flight time behavior in the carbon foil time pick-up detector

Mikko Laitinen, Mikko Rossi, Jaakko Julin and Timo Sajavaara

Submitted to: Nucl. Instr. and Meth. A

[III] Trajectory bending and energy spreading of charged ions in time-of-flight telescopes used for ion beam analysis

Mikko Laitinen and Timo Sajavaara

Submitted to: Nucl. Instr. and Meth. B

[IV] Depth profiling of Al_2O_3 + TiO_2 nanolaminates by means of a time-of-flight energy spectrometer;

Mikko Laitinen, Timo Sajavaara, Mikko Rossi, Jaakko Julin, Riikka L. Puurunen, Tommi Suni, Tadashi Ishida, Hiroyuki Fujita, Kai Arstila, Bert Brijs, Harry J. Whitlow.

Nucl. Instr. and Meth. B 269 (2011), pp. 3021-3024.

http://dx.doi.org/10.1016/j.nimb.2011.04.074

[V]   ALD Grown Aluminum Oxide Submonolayers in Dye-Sensitized Solar Cells: The Effect on Interfacial Electron Transfer and Performance;

Liisa J. Antila, Mikko J. Heikkilä, Ville Mäkinen, Niko Humalamäki, **Mikko Laitinen**, Veikko Linko, Pasi Jalkanen, Jussi Toppari, Viivi Aumanen, Marianna Kemell, Pasi Myllyperkiö, Karoliina Honkala, Hannu Häkkinen, Markku Leskelä, and Jouko E. I. Korppi-Tommola

J. Phys. Chem. C, 115 (2011), pp 16720–16729.

http://dx.doi.org/10.1021/jp204886n

Author's contribution

In [I] author has designed, assembled, constructed and tested the ToF-ERDA spectrometer. Author has performed nearly all the measurements and written the draft of the paper, figures included. For [II] and [III] author has made the experimental work, simulations and written the draft of the paper with figures included. For [IV] author made the ToF-ERDA measurements, data analysis and wrote the draft of the paper with figures included. In [V] author has made the ToF-ERDA measurements and analysis of Al and H concentrations on top of the TiO_2 film.

Other peer reviewed publications from the author

1. Atomic layer deposition of $Li_xTi_yO_z$ thin films, V. Miikkulainen, O. Nilsen, **M. Laitinen**, T. Sajavaara, H. Fjellvåg, RSC Adv., 3 (2013), p. 7537, http://dx.doi.org/10.1039/c3ra40745d.

2. Energy-loss straggling of 2–10 MeV/u Kr ions in gases, C. Vockenhuber, J. Jensen, J. Julin, H. Kettunen, **M. Laitinen**, M. Rossi, T. Sajavaara, O. Osmani, A. Schinner, P. Sigmund, Eur. Phys. J. D, 67 (2013), p. 1, http://dx.doi.org/10.1140/epjd/e2013-40095-4.

3. Advanced time-stamped total data acquisition control front-end for MeV ion beam microscopy and proton beam writing, H. Kivistö, M. Rossi, P. Jones, R. Norarat, N. Puttaraksa, T. Sajavaara, **M. Laitinen**, V. Hänninen, K. Ranttila, P. Heikkinen, Microelectron. Eng., 102 (2013), p. 9, http://dx.doi.org/10.1016/j.mee.2012.02.011.

4. Why are hydrogen ions best for MeV ion beam lithography? R. Norarat, N. Puttaraksa, M. Napari, A. Ananda Sagari, **M. Laitinen**, T. Sajavaara, P. Yotprayoonsak, M. Pettersson, O. Chienthavorn, H.J. Whitlow, Microelectron. Eng., 102 (2013), p. 22, http://dx.doi.org/10.1016/j.mee.2012.02.012.

5. Production of pure samples of ^{131m}Xe and ^{135}Xe, K. Peräjärvi, T. Eronen, A. Cagniant, D. Gorelov, J. Hakala, A. Jokinen, A. Kankainen, H. Kettunen, V.S. Kolhinen, **M. Laitinen**, I.D. Moore, H. Penttilä, J. Rissanen, A. Saastamoinen, H. Toivonen, J. Turunen, J. Äystö, Appl. Radiat. Isotopes, 71 (2013), p. 34, http://dx.doi.org/10.1016/j.apradiso.2012.09.007.

6. Influence of titanium-substrate roughness on Ca-PO thin films grown by atomic layer deposition, A. Sagari, J. Malm, **M. Laitinen**, P. Rahkila, M. Hongqiang, M. Putkonen, M. Karppinen, H.J. Whitlow, T. Sajavaara, Thin Solid Films, 26 (2012), p. 26, http://dx.doi.org/10.1016/j.tsf.2012.11.137.

7. Atomic layer deposition of Ru films from bis (2, 5-dimethylpyrrolyl) ruthenium and oxygen, K. Kukli, J. Aarik, A. Aidla, I. Jõgi, T. Arroval, J. Lu, T. Sajavaara, **M. Laitinen**, A. Kiisler, M. Ritala, Thin Solid Films, 520 (2012), p. 2756, http://dx.doi.org/10.1016/j.tsf.2011.11.088.

8. Development of the Jyväskylä microbeam facility, R. Norarat, T. Sajavaara, **M. Laitinen**, P. Heikkinen, K. Ranttila, K. Ylikorkala, V. Hänninen, M. Rossi, P. Jones, V. Marjomäki, Nucl. Instr. and Meth. B, 272 (2012), p. 158, http://dx.doi.org/10.1016/j.nimb.2011.01.055.

9. Lithography exposure characteristics of poly (methyl methacrylate)(PMMA) for carbon, helium and hydrogen ions, N. Puttaraksa, R. Norarat, **M. Laitinen**, T. Sajavaara, S. Singkarat, H.J. Whitlow, Nucl. Instr. and Meth. B, 272 (2012), p. 162, http://dx.doi.org/10.1016/j.nimb.2011.01.056.

10. Plasma etch characteristics of aluminum nitride mask layers grown by low-temperature plasma enhanced atomic layer deposition in SF_6 based plasmas, A. Perros, M. Bosund, T. Sajavaara, **M. Laitinen**, L. Sainiemi, T. Huhtio, H. Lipsanen, J. Vac. Sci. and Tech. A, 30 (2012), p. 011504, http://dx.doi.org/10.1116/1.3664306.

11. P. Ujić, A. Lagoyannis, T. J. Mertzimekis, F. de Oliveira Santos, S. Harissopulos, P. Demetriou, L. Perrot, C. Stodel, M. Saint-Laurent, O. Kamalou, A. Lefebvre‐Schuhl, A. Spyrou, M. A. Amthor, S. Grevy, L. Caceres, H. Koivisto, **M. Laitinen**, J. Uusitalo, and R. Julin, in AIP Conference Proceedings, 2011), p. 321.

12. Porous inorganic–organic hybrid material by oxygen plasma treatment, S. Aura, V. Jokinen, **M. Laitinen**, T. Sajavaara, S. Franssila, J. Micromech. Microengineering, 21 (2011), p. 125003, http://dx.doi.org/10.1088/0960-1317/21/12/125003.

13. Properties of AlN grown by plasma enhanced atomic layer deposition, M. Bosund, T. Sajavaara, **M. Laitinen**, T. Huhtio, M. Putkonen, V. Airaksinen, H. Lipsanen, Appl. Surf. Sci., 257 (2011), p. 7827, http://dx.doi.org/10.1016/j.apsusc.2011.04.037.

14. Direct Writing of Channels for Microfluidics in Silica by MeV Ion Beam Lithography, N. Puttaraksa, M. Napari, O. Chienthavorn, R. Norarat, T. Sajavaara, **M. Laitinen**, S. Singkarat, H.J. Whitlow, Adv. Mat. Res., 254 (2011), p. 132, http://dx.doi.org/10.4028/www.scientific.net/AMR.254.132.

15. Controlling the crystallinity and roughness of atomic layer deposited titanium dioxide films, R.L. Puurunen, T. Sajavaara, E. Santala, V. Miikkulainen, T. Saukkonen, **M. Laitinen**, M. Leskela, J. Nanosci. Technol., 11 (2011), p. 8101, http://dx.doi.org/10.1166/jnn.2011.5060.

16. Atomic layer deposition of ruthenium films from (ethylcyclopentadienyl)(pyrrolyl) ruthenium and oxygen, K. Kukli, M. Kemell, E. Puukilainen, J. Aarik, A. Aidla, T. Sajavaara, **M. Laitinen**, M. Tallarida, J. Sundqvist, M. Ritala, M. Leskelä, J. Electrochem. Soc., 158 (2011), p. D158, http://dx.doi.org/10.1149/1.3533387.

17. Ultra-high resolution mass separator—Application to detection of nuclear weapons tests, K. Peräjärvi, T. Eronen, V. Elomaa, J. Hakala, A. Jokinen, H. Kettunen, V. Kolhinen, **M. Laitinen**, I. Moore, H. Penttilä, Appl. Radiat. Isotopes, 68 (2010), p. 450, http://dx.doi.org/10.1016/j.apradiso.2009.12.020.

18. Development of micro-contact printing of osteosarcoma cells using MeV ion beam lithography, S. Sangyuenyongpipat, V. Marjomäki, S. Ikonen, T. Sajavaara, A. Ananda Sagari, S. Gorelick, **M. Laitinen**, H.J. Whitlow, Nucl. Instr. and Meth. B, 267 (2009), p. 2306, http://dx.doi.org/10.1016/j.nimb.2009.03.018.

19. Fabrication of microfluidic devices using MeV ion beam Programmable Proximity Aperture Lithography (PPAL), S. Gorelick, N. Puttaraksa, T. Sajavaara, **M. Laitinen**, S. Singkarat, H. Whitlow, Nucl. Instr. and Meth. B, 266 (2008), p. 2461, http://dx.doi.org/10.1016/j.nimb.2008.03.035.

20. Programmable proximity aperture lithography with MeV ion beams, N. Puttaraksa, S. Gorelick, T. Sajavaara, **M. Laitinen**, S. Singkarat, H.J. Whitlow, Nucl. Instr. and Meth. B, 26 (2008), p. 1732, http://dx.doi.org/10.1016/j.nimb.2008.03.035.

21. Wettability and compositional analysis of hydroxyapatite films modified by low and high energy ion irradiation, A. Ananda Sagari, P. Rahkila, M. Väisänen, R. Lehto, T. Sajavaara, S. Gorelick, **M. Laitinen**, M. Putkonen, S. Sangyuenyongpipat, J. Timonen, Nucl. Instr. and Meth. B, 266 (2008), p. 2515, http://dx.doi.org/10.1063/1.2196481.

22. Mobility determination of lead isotopes in glass for retrospective radon measurements, **M. Laitinen**, I. Riihimäki, J. Ekman, A.A. Sagari, L.B. Karlsson, S. Sangyuenyongpipat, S. Gorelick, H. Kettunen, H. Penttilä, R. Hellborg, Radiat. Prot. Dosimet., 131 (2008), p. 212, http://dx.doi.org/10.1093/rpd/ncn162.

23. Ion-sputtering deposition of Ca–P–O films for microscopic imaging of osteoblast cells, A. Ananda Sagari, C. Lautaret, S. Gorelick, **M. Laitinen**, P. Rahkila, M. Putkonen, K. Arstila, T. Sajavaara, S. Cheng, H.J. Whitlow, Nucl. Instr. and Meth. B, 261 (2007), p. 719, http://dx.doi.org/10.1016/j.nimb.2007.03.100.

24. Development of an MeV ion beam lithography system in Jyväskylä, S. Gorelick, T. Ylimäki, T. Sajavaara, **M. Laitinen**, A. Sagari AR, H.J. Whitlow, Nucl. Instr. and Meth. B, 260 (2007), p. 77, http://dx.doi.org/10.1016/j.nimb.2007.01.260.

Table of Contents

1   INTRODUCTION

What are the concentrations of different elements in my sample? This is the question asked by many. To find out the answer to this question a single measurement or in many cases several measurements need to be performed. The elemental analysis of the solid materials can be done in multiple ways. Many of the available methods are more familiar from the chemistry side where different optical (UV to IR) methods from emission and absorption to fluorescence are common. Other typical methods are based on separating different masses, many times after a different ionization process such as inductively coupled mass spectrometry. Elemental information can also be obtained from the inner electron structure of the atoms by means of proton induced X-ray emission, X-ray fluorescence, photoelectrons or Auger electrons. [1]

However, all the above mentioned methods are qualitative, or in the best case semi-quantitative, without high quality reference samples thus probing only the relative atomic concentrations of the sample and also often lack the possibility for direct detection of hydrogen. The number of quantitative methods which do not need any reference sample for the elemental concentration analysis is very limited. These include different neutron induced or ion beam analysis techniques such as Rutherford backscattering spectrometry (RBS) by which all the sample elements, excluding hydrogen, can be quantified. In most cases RBS provides simultaneously also depth information of the elemental concentrations. The only clear drawback of the ion beam analysis is the need for high energy ion beam, often in a few MeV region, which is delivered by a physically large ion source-accelerator-beam tube -construction. Another issue of ion beam methods is that the probing depth of the sample is limited. However, this is also an enormous advantage when thin films of few 100 nm thick to less than one atomic layer "thick" films are required to be analyzed.

The limitation of the RBS method, the inability to measure the hydrogen concentration from the sample, can be overcome when elastic recoil detection (ERD) in forward scattering angle is used. When both the velocity and the energy are measured for all the particles the energetic heavy ion beam kicks (or recoils) out of the sample towards the detector, the mass of all particles can be determined. This method is called a Time-of-Flight – Elastic Recoil Detection Analysis (ToF-ERDA) (see Fig. 1.1).
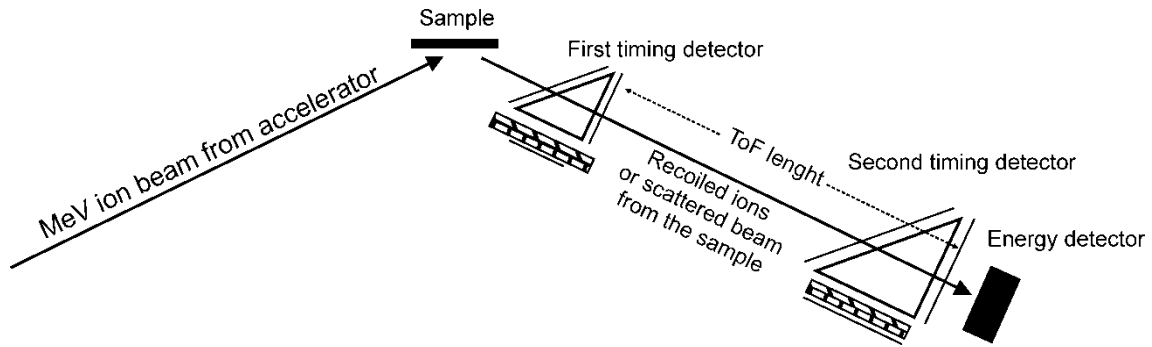
Figure 1.1: Schematic of the Time-of-flight – Elastic Recoil Detection Analysis (ToF-ERDA) setup.

The timing detectors used in the Jyväskylä ToF-ERDA tool are of transmission type providing the start and the stop signal over a known distance between detectors, and from these the velocity of the particle can be calculated. The timing detectors are so called carbon foil time pick-up detectors (for short: timing gates) introduced by Busch et al. [2]. Although they can be used for all ions and energies, even down to few tens of keVs [3] they have some known limitations. The detection efficiency is, for example in the case of hydrogen, proportional to the stopping force of the carbon foil acting to the passing ion and the efficiency is often less than 100 % for the lightest ions (see for example [4]). Other known limitations are the ion scattering in the carbon foils [5] and the tandem effect [6] which limits the energy resolution in certain timing gate voltage configurations for energies lower than ~1 MeV.
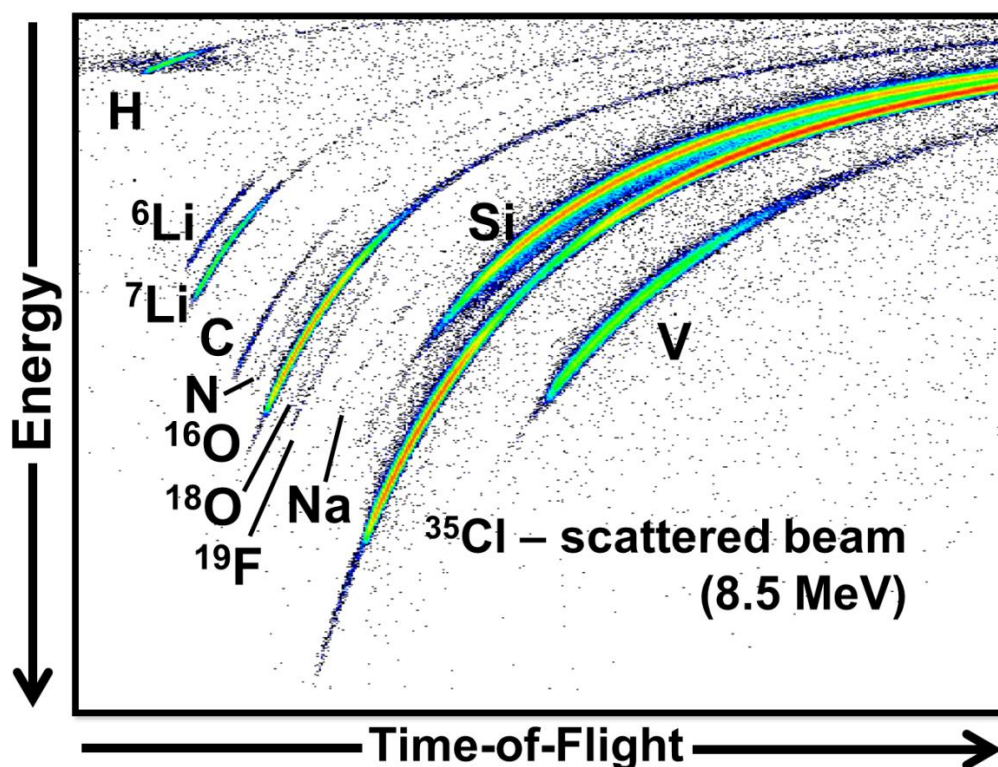
Figure 1.2: ToF-ERDA histogram of ~100 nm thick atomic layer deposited $Li_xV_yO_z$ thin film on a Si substrate [7].

Typically in a ToF-ERDA measurement the coincident time-of-flight and energy information is used to separate different masses visible in different isobaric curves, also called as "banana curves" (see Fig. 1.2 for example). From the ToF and E data only the time-of-flight information is usually used when the elemental depth profiles are later calculated. Timing gate performance and the timing resolution hence directly impacts the achievable depth resolution.

The aim of this work was to build a ToF-ERDA telescope with sub-nm depth resolution, high detection efficiency and low background for lower detection limit while being also reliable and easy to use in everyday measurements. Within this work a ToF-ERDA spectrometer was designed, constructed, assembled and taken in to use in the Accelerator Laboratory of the University of Jyväskylä. Over the past few years hundreds of thin film samples have been measured and quantitative elemental depth profiles have been provided for several Finnish and international collaborators. This thesis mainly focuses on the timing gates, their properties and the impact to the ToF-ERDA performance. The whole ToF-ERDA system and its figures of merit are also described. Results obtained with the help of simulations of the halo structures seen around light isotopic curves at the ToF-E histograms (also seen around the hydrogen in Fig. 1.2) and simulated time spreads caused by the tandem effect are also discussed. Other background generating events, as present also in the ToF-E histogram in Fig. 1.2 are discussed more detailed in [I].

2 TIME OF FLIGHT - ELASTIC RECOIL DETECTION ANALYSIS

Purpose of this chapter is to shortly introduce the time of flight - elastic recoil detection analysis method which is most often used for depth profiling and elemental analyses of thin films. This is done by introducing the detectors and equipment used in the field and by presenting the underlying theory. Therefore, sub-chapters discuss ToF-ERDA's historical development with the actual detectors involved and the theory behind the principles of the method.

2.1 Brief history of the ToF-ERDA

Elastic recoil detection analysis ERDA was first time used in 1976 for determining the depth distribution of light elements in heavy materials by L'Ecuyer [8] from the University of Montreal. Then surface barrier silicon detector was commonly used as the energy detector. In ERDA an absorber foil in front of the detector was used to discriminate the scattered incident beam hitting the detector. Later, in 1983, also ToF version of the ERD measurements was first time reported [9] which did not yet fully combine both the timing and energy measurements in coincidence.

In the timing detectors, generation of fast timing signals from the passing particles by the secondary electrons emitted from the metallic foil was already used in the late 1950's [10]. Other types of timing detectors, where particle has directly hit to the scintillation or surface barrier detector have been used for the timing of heavy ions as well [11]. The isochronous electron transport for timing detectors by magnetic field was first introduced by Zebelman et al. in 1977 [12] (see Fig. 2.1) and in 1980 by Busch et al. by using an electric field [2] (see Fig. 2.2). These detectors started to gain ground over the earlier detector designs using tilted carbon foil and direct secondary electron paths (see Fig. 2.3).

The timing detector type presented by Busch et al. (see Fig. 2.2) is still actively in use also today in nuclear physics and in most modern ToF-ERDA tools. The only drawback in it is the grid design and the requirement of three grids for one timing gate which reduces the transmission of ions. These issues are discussed in more detail in chapter 4.
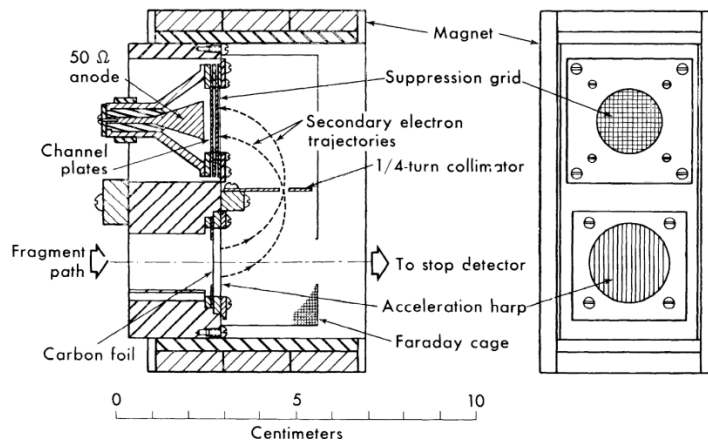
Figure 2.1: Timing detector with isochronous electron transport based on a magnetic field. From Zebelman et al. 1977 [12], used with permission from Elsevier.
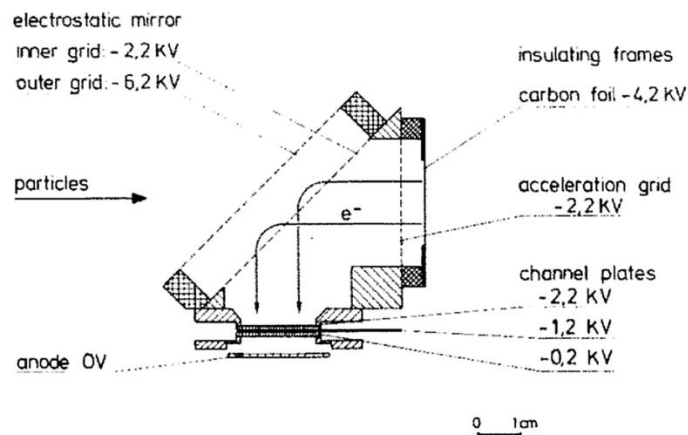

Figure 2.2: Timing detector with isochronous electron transport based on a electric field. From Busch et al. 1980 [2] , used with permission from Elsevier.
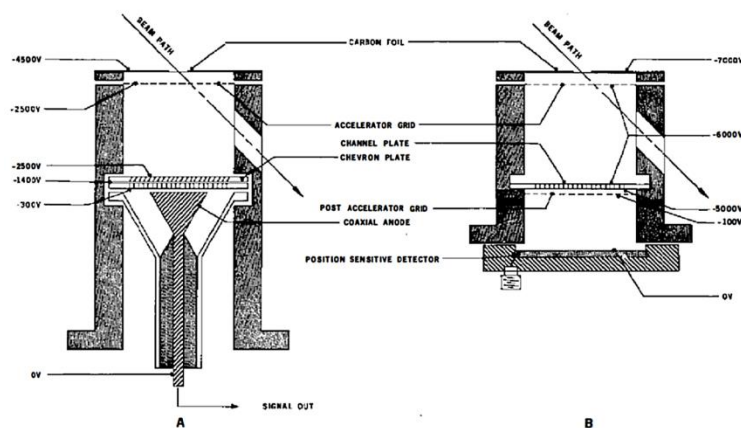

Figure 2.3: Timing detector designs where foil is not perpendicular to the incident beam. The electron paths, however, are straight from the foil to the channel plate. From Identification of nuclear particles, Fred S. Goulding and Bernard G. Harvey, 1975 [13], used with permission from Annual Reviews.

The ERD technique in which both the ToF and E events are measured in coincidence, was introduced in University of Montreal in 1983 [14] for quantitative elemental depth profiling. Their system utilized only one transmission timing detector, similar to the ones in Fig. 2.3, and the second timing event was recorded from the energy detector, together with the energy signal. In order to reduce the ToF count rate, the signal from the first detector was delayed so that the timing started from the energy detector signal. By measuring both the energy E and velocity v for an individual ion and by using the simple formula

$$E = \tfrac{1}{2}mv^2, \tag{1}$$

different masses m could be identified from the collected data. This was not previously possible as in the traditional ERD, the particles having the same energy (or velocity in ToF-detection) but different masses overlapped in the energy spectrum. Thus discrimination of the velocity and the energy of the individual particles is needed for reliable identification as suggested also in [9].

Other methods for the identification of recoiled species are discussed, for instance, in [15]. The identification can be done using magnetic, electromagnetic, momentum-energy or ΔE-E detectors. In [15] the main emphasis is given for the ToF-E method which does not suffer the effects of the entrance window of the ΔE-E method and is charge-state independent. In Ref. [15], is also presented one of the first ToF-ERDA coincidence histograms with isobaric mass-curves of different elements. Practically similar histograms are regularly used today among the ToF-ERDA researchers as it is a convenient way to express the raw coincident ToF-E data (see Fig. 2.4 for instance).
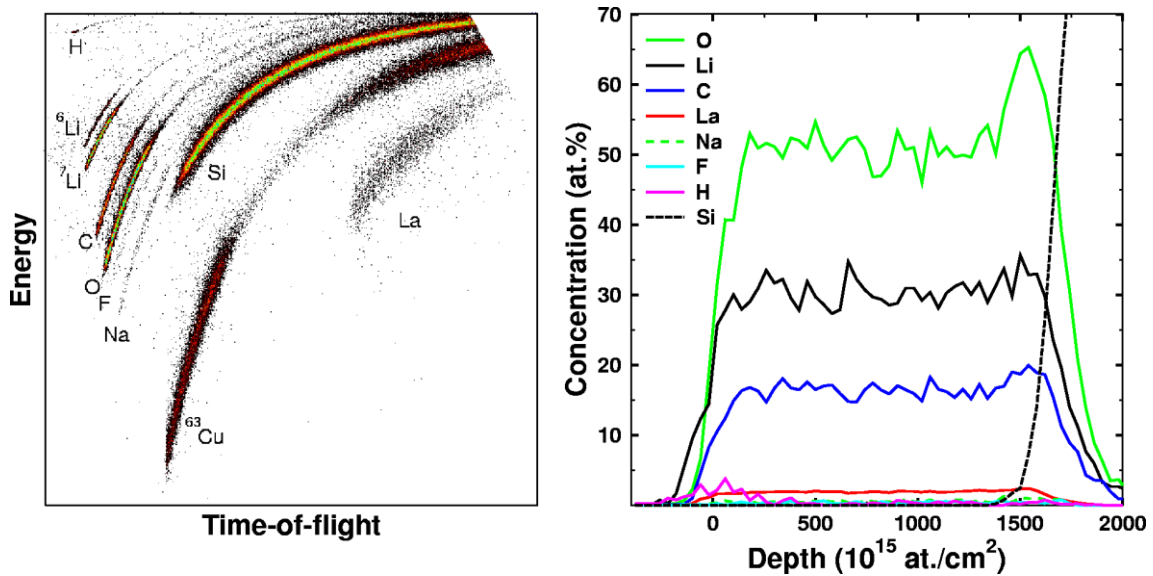
Figure 2.4: A raw ToF-ERDA histogram on the left and depth profile calculated from the data on the right. The thickness of the film containing mainly oxygen, lithium and lanthanum is 144 nm. Sample was measured with the ToF-ERDA telescope described in [16]. From [17], used with permission from Elsevier.

Since the 1980s, the quantitative depth profiling of elements by ToF-ERDA method has evolved in smaller steps. As thin films have really got 'thin', from nanometers to even sub-monolayers [V], also ion beam energies have decreased from the tens of MeVs to a few MeV used today for the thinnest films. Smaller ion beam energies are advantageous not only in eyes of physics where cross sections, stopping force and the relative energy loss in the film play important role, e.g. hydrogen detection is often more efficient at lower energies, but are important also for the sheer simplicity of the equipment needed. Older building sized accelerators are not needed anymore for the thin film analysis but the accelerators capable of producing a few MeV heavy ions beams now fit in a single room, which is also an improvement in the economical side. Another improvement has been the development of the computer-based data-acquisition, first in a list mode (used for the data also in Fig. 2.4) and later with the advanced time-stamping properties. Very significant recent development has been the utilization of gas ionization detectors with thin Si_3N_4 entrance windows as replacements for the ion implanted silicon energy detectors [18]. ToF-ERDA tools with improved position sensitive detectors are also needed when large solid angle and the resulting kinematic spread is taken into account [19,20] to achieve the improved depth resolution. All of these more recent hardware related developments are also discussed later in this thesis.

2.2   Physics behind the elemental depth profiles

In this sub-chapter a short introduction is given to the theory and theoretical terms behind the physics in the quantitative elemental depth profiling with ToF-ERDA. More detailed theory sections relevant to the field can be found from other sources starting from [21--25]. These sources are also used as general references on this chapter. Useful and more detailed theory overviews are also presented on many theses [26--29] related to ToF-ERDA.

2.2.1   Kinematics of the binary collisions

In the elastic two body collision the energy transfer from the incident particle to the target nucleus can be calculated from the laws of the conservation of energy

$$E_0 \equiv \tfrac{1}{2}M_i v_0^2 = \tfrac{1}{2}M_i v_i^2 + \tfrac{1}{2}M_r v_r^2 \tag{2}$$

and from the conservation of momentum

$$M_i v_0 = M_i v_i \cos\theta + M_r v_r \cos\phi \ , \tag{3}$$

$$0 = M_i v_i \sin\theta - M_r v_r \sin\phi \ , \tag{4}$$

where M_i and M_r are masses of the *incident* and the *recoiled* particles, v is the velocity and angles θ and ϕ as represented in Fig. 2.5. In general, elastic collision approximation holds well in the ion beam analysis.

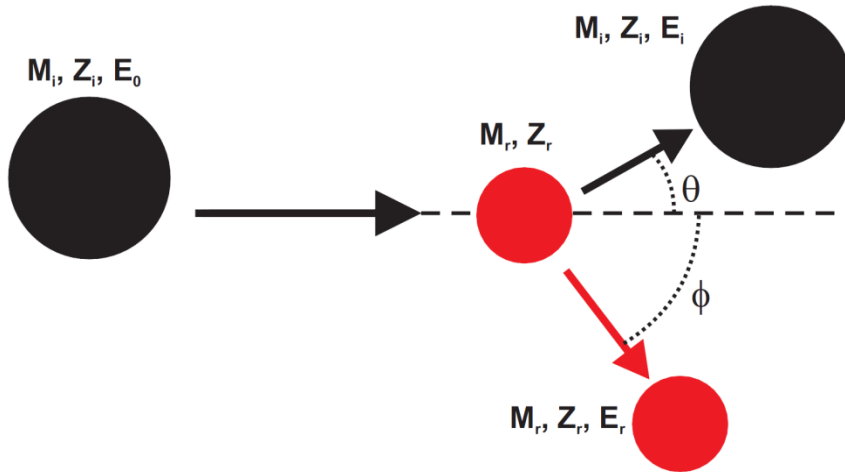

Figure 2.5: Binary collision. Kinematics, i.e. energies at known angles, can be calculated for the scattered incident particle M_i, Z_i, E_i and recoiled particle M_r, Z_r, E_r from the laws of conservation of energy and momentum in elastic two body collisions.

By defining the ratio of the incident particle energy after and before the collision, we get

$$K = \frac{E_i}{E_0}, \tag{5}$$

where K is the so called kinematic factor for the incident particle. In backscattering, and forward scattering spectrometry which is used together with the ToF-ERD, this kinematic factor can be written by using (2), (3), (4)and (5) as a

$$K \, E_0 = \left(\frac{\pm\sqrt{M_r{}^2 - M_i{}^2 \sin^2\theta} + M_i \cos\theta}{M_i + M_r} \right)^2 E_0 = E_i \equiv E_0 - E_r \, . \tag{6}$$

Here (6) E_r is the energy of the recoiled particle. If the incident ion mass M_i is larger than the recoiling mass M_r, the scattered incident particle can be detected at two different energies, at the same scattering angle. However, the scattering cross section, discussed below, is different for the two different energies. The recoiling particle energy E_r can be written in a form

$$E_r = \left(\frac{4 \, M_i \, M_r \cos^2\phi}{(M_i + M_r)^2} \right) E_0 \equiv \Lambda \, E_0 \, , \tag{7}$$

where Λ is the kinematic factor for the recoiled particle. In the case of the ERD measurement only one detector angle, $\theta = \phi$, is generally used.

2.2.2 Scattering cross section

The previous section established a connection between the incident energy and the energy of the particle after the elastic collision and detection at an angle of θ. The probability, or frequency, of such collision to take place is expressed by the differential scattering cross section

$$d\sigma/d\Omega = \left(\frac{1}{Nt} \right) \left[\left(\frac{dQ}{d\Omega} \right) / Q \right] , \tag{8}$$

where N is the volume density of atoms in the target and t is its thickness, dQ is the number of particles scattering to the detector, $d\Omega$ is the differential solid angle of the detector and Q is the number of particles incident in the target.
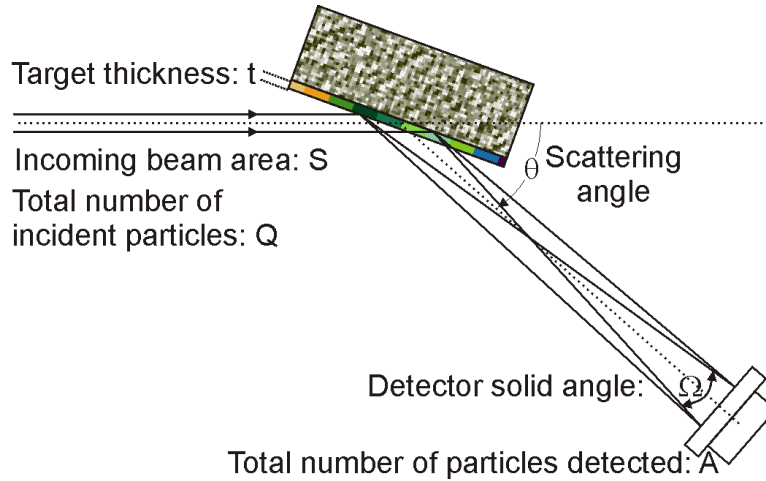

Figure 2.6: Schematic view of the ERDA setup regarding to the cross section.

To calculate the differential cross section for an elastic collision, conservation of both energy and momentum need to be taken into account by a specific model for the force that acts during the collision between the incident particle and target masses. In simplest cases the Coulomb repulsion can be used with the closest approach model and the differential scattering cross section for incident particle can be written in the laboratory coordinates

$$\frac{d\sigma_i}{d\Omega} \cong \left(\frac{Z_i Z_r e^2}{8\pi\varepsilon_0 E_0}\right)^2 \frac{1}{\sin^4\theta} \frac{\left\{\sqrt{1-((M_i/M_r)\sin\theta)^2}+\cos\theta\right\}^2}{\sqrt{1-((M_i/M_r)\sin\theta)^2}} \tag{9}$$

and similarly for the recoiled particle

$$\frac{d\sigma_r}{d\Omega} \cong \frac{\left[Z_i Z_r e^2 (M_i+M_r)\right]^2}{(8\pi\varepsilon_0 E_0 M_r)^2 \cos^3\theta} \tag{10}$$

These are known also as Rutherford cross sections. In (9) and (10) the angle θ refers to the Fig. 2.6, as in Fig. 2.5 the angle for recoiled and scattered particle is defined separately. When scattering angle θ and the solid angle Ω are well defined by the instruments and the scattering cross section σ is known or can be calculated, the number of target atoms per unit area can be written in a form

$$A = \sigma\,\Omega * Q * N\,t. \tag{11}$$

$$\begin{pmatrix} number\ of \\ detected\ particles \end{pmatrix} = \sigma\,\Omega * \begin{pmatrix} total\ number\ of \\ incident\ particles \end{pmatrix} * \begin{pmatrix} number\ of\ target \\ atoms\ per\ unit\ area \end{pmatrix}$$

Using the formulas (9) (10) (11) with a known solid angle, it is now possible to quantify the sample surface atom concentrations from an experimental data. To quantitatively depth profile the sample atoms beneath the surface, the energy loss of ions traversing the material must be taken in to account. This ion energy loss is caused mainly by the interactions with electrons and it is expressed as stopping force which is a material property for the specific ion.

2.2.3   Stopping force

Theoretical framework of the stopping force dE/dx acting to the energetic particle travelling in the matter originates from the works of Bethe, Bloch and Bohr [30--33]. The general formula for the electronic stopping for the energetic particle, projectile, travelling through the matter has a form of

$$-\frac{dE}{dx}\bigg|_{elec.} = N\,Z_2 S \tag{12}$$

$$= \frac{1}{4\pi\varepsilon_0}\frac{Z_1^2 e^4}{m_e v^2} N Z_2 L, \tag{13}$$

where

N	is the atomic density of the target material,
S	is the electronic stopping cross-section in units of [energy × area],
$Z_{1,2}$	are the atomic numbers for the projectile (1) and target (2),
ε_0	is the vacuum permittivity,
e and m_e	are the elementary charge and the electron rest mass, respectively,
v	is the velocity of the projectile and
L	is the dimensionless theory dependent[1] stopping number.

Formula (12) describes the projectile energy loss per unit length caused by the collisions between the ion and target electrons. In reality also nuclear interactions/collisions occur and cannot be rejected for low projectile velocities. Coulombic interactions between the projectile and the target nuclei can similarly be treated as an energy loss per unit length

$$-\frac{dE}{dx}\bigg|_{nucl.} = \frac{1}{4\pi\varepsilon_0}\frac{Z_1^2 Z_2^2 e^4}{M_2 v^2}\mathrm{N}L_{nucl.}. \tag{14}$$

For high projectile velocities nuclear stopping can be several orders of magnitude lower than the electronic stopping but once the projectile velocity approaches the Bohr velocity (electron velocities) its significance grows rapidly. Energies related to the ToF-ERD measurements performed with the Pelletron accelerator of the University of Jyväskylä can be considered to range from less than 100 keV to 20 MeV. For these energies, the electronic stopping is always clearly dominant for projectiles lighter than silicon but in the case of heavier projectiles nuclear stopping force cannot be completely neglected.

---

[1] In case of the Bethe formula $L = \ln\left(\frac{2m_e v^2}{I}\right)$, where I is the mean energy required to ionize an atom in the medium. This is difficult to calculate and is, in practice, often approximated as $Z_2 \times 11$ eV [34].

2.2.4   Other factors affecting the ToF-ERDA results

While the kinematics, the cross sections and the stopping forces are the key physical properties of the ToF-ERDA measurements there are also several other factors contributing the final results. In the following some of them are discussed in the view of their relevance to the energy region in use or to the specific equipment built during this work. It is also worth to notice that some of these other physical factors are in fact tightly related to the physics discussed and the general references to the theory mentioned above.

The kinematics, which defines the energy of a particle scattered towards a certain angle, often causes the largest energy spread to the results in the current measurement systems. This spread in the detected energy values is caused by *the kinematic spreading* to different solid angles of the detector (see also Fig. 2.7). The spreading is largest for the recoiled sample atoms. Because the exact recoil/scattering angle is not measured for all ions individually, the width of the spread depends from the diameter (solid angle) of the detector. To give an example of the kinematic spreading with the parameters of the Jyväskylä design presented in this thesis, by using (7) and the known geometry, one can calculate the maximum spread for the recoiled energies and come up to a number of more than 2.5 % difference in the actual recoiled energies which are assumed to be identical in the analysis.
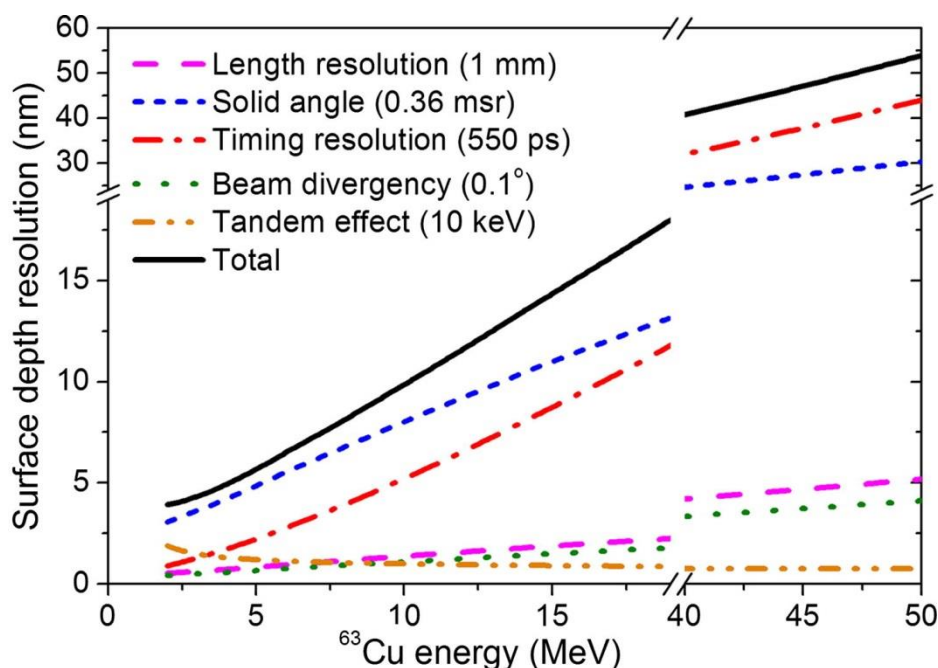

Figure 2.7: Example of different contributions to the surface depth resolution obtained from the ToF detector in case of O recoiled by ^{63}Cu beam incident on Si. From [35], used with permission from Elsevier.

The kinematic spreading is a well-known and also a constant so it can be more easily tolerated. *The screening effect of the scattering cross section* can, however, produce a incorrect elemental ratios, which is often far more critical to the final results. The screening effect takes place when the scattering cross section for the target and the projectile cannot be calculated from the pure Coulombic interaction between the two nuclei but also the effect of the electron clouds need to be considered. Different corrections to the Rutherford scattering cross section σ_R (equations (9) and (10)) has been presented, one of them by L'Ecuyer et al. [36]

$$\frac{\sigma}{\sigma_R} = 1 - \frac{0.049\, Z_1\, Z_2{}^{4/3}}{E_{CM}}, \qquad (15)$$

where E_{CM} refers to the center-of-mass kinetic energy. This (15) approximation, however, performs well only with lighter ions, such as helium and is less practical in ToF-ERDA with heavy ions. Another similar correction is presented by Andersen et al. where also angular dependence is included [37].

Straggling has its origin in the statistical nature of the energy loss processes, and is observed as an energy spread after energy loss processes, hence straggling shows as a second order effect of the stopping force. One example of the straggling occurs when ions pass the carbon foil of the first timing detector. Here all ions suffer the effect of the carbon foil on both terms of stopping and straggling. The magnitude of the straggling in the 3 μg/cm² (~13 nm) carbon foil is for example for the 250 keV He ions ~2 keV while the energy loss is about 5 keV (by SRIM [38] calculations).

Another effect which can distort the inferred elemental compositions is *the multiple scattering* (or *MS)*. The basic assumption in all the ion beam analysis techniques is that the scattered ion or recoil ends up to the detector as a result of single scattering. This is not always the case when low energy heavy ions and thin films containing heavy elements are involved, but there can be multiple scattering on the way of the incident ions and recoils before they are emitted towards the detector from the sample. Monte Carlo -simulations, such as MCERD [5], are often required to obtain reliable impurity concentration for a thin film surrounded by a strong surface and interface impurity peaks.

Sometimes overlooked effect which can have a large effect to the ToF-ERDA results is *the ion irradiation induced composition change* during the measurement [39]. This effect mostly concerns light volatile elements under ion bombardment, but depends significantly on the sample properties. The composition changes can be taken into account in the offline analysis if the DAQ system collects the events in a list mode. This type of correction in the offline data analysis can be easily performed, for example, by using the Potku [40] software, a tool developed in Jyväskylä to analyze the ToF-E histograms and to calculate depth profiles and elemental compositions from the measured data.

Final effect to mention, and to be minimized, is *the tandem effect*. The origin of this effect is often [6,20,41--43] referred to the high electric potential of the carbon foil in the first timing gate (see also Fig. 2.7). The magnitude of this effect to the measured energy (by ToF) can be approximated directly by $\overline{\Delta E} = \overline{\Delta q} * V$, where Δq is the charge state difference of the ion before and after the foil and V is the potential of the first carbon foil. This extra spread of the measured ToF can be reduced by decreasing the potential, or grounding, the first carbon foil. Although the effect is real, it is more complicated than presented by this simple formula. Tandem effect is discussed in detail in the chapter 4.2.1 utilizing computer simulations. [III]

3 DESIGN AND CONSTRUCTION OF THE JYVÄSKYLÄ TOF-ERDA SETUP

3.1 Beam line, measurement chamber and the sample stage

The ToF-ERDA setup was installed to the +15 degree beamline of the 1.7 MV Pelletron accelerator at the Accelerator Laboratory of the University of Jyväskylä [I]. A choice of +30 degrees beamline would have also been possible from the analyzing magnet if the existing RBS beamline would have been moved off first (see Fig. 3.1). The mass and energy selectivity would have been better at +30 degrees but the magnet, originally intended only for H and He beams, is somewhat weak, and the +15 degree beamline enables the use of more charge states for a single terminal voltage. Considering also the space limitations, the +15 degrees beamline was finally selected.
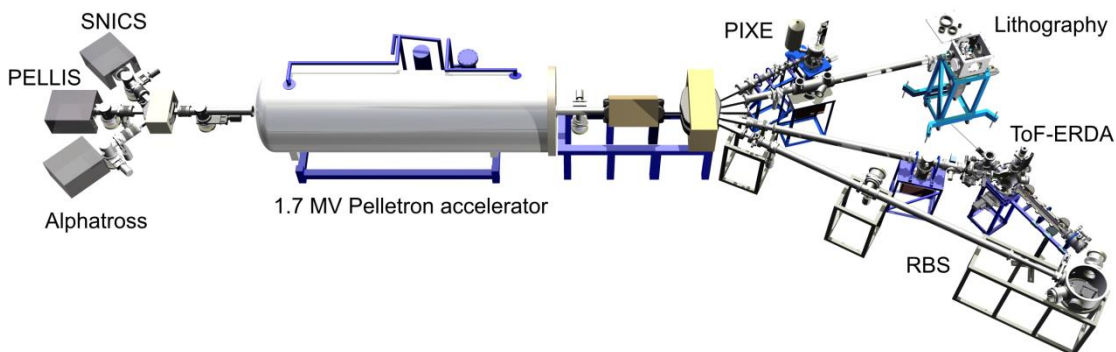

Figure 3.1: Pelletron accelerator, ion sources and beamlines as of 2013.

A beam profile monitor and X-Y slits were installed to the beamline to allow for tuning and monitoring the ion beam. The slits can be seen at the lower left corner of the Fig. 3.2. Gate valves right after the analyzing magnet and before the chamber improve the maintenance options and the small gate valve before the chamber is often used also as a beam stop before the individual measurement is started. The beamline is pumped with an ion pump sharing the control unit with an identical ion pump in the lithography beamline.
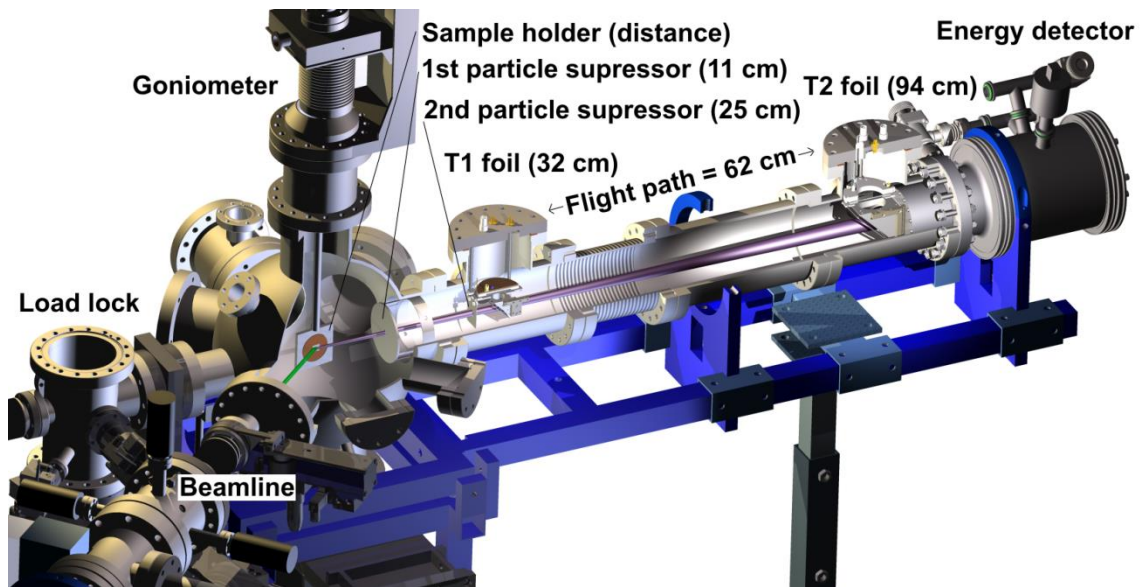
Figure 3.2: ToF-ERDA beamline, load lock, chamber with the goniometer and the telescope arm with two timing detectors and an energy detector.

For fast sample changes a load lock with a turbo pump was attached to the measurement chamber (left in the Fig. 3.2). The load lock also reduces contamination of the main chamber and the telescope system by allowing to keep them permanently in high vacuum. During the sample change the pumping steps of the load lock take around 2 and 4 minutes for the rough and turbo pumping, respectively.

The spherical measurement chamber, with all CF flanges, is adopted from an old sputtering setup. The base vacuum of the system is typically 2E-8 mbar which is reached with few non-metal seals and without baking. Although the main chamber has many ports allowing for modifications and future options, a small disadvantage is that the goniometer, and the sample to be analyzed, locate at the center of the largish (diameter 30 cm) chamber. As it is not feasible to position the first timing gate inside the chamber, the ToF-distance, or the solid angle of the system, is therefore reduced from the optimal configuration where the T1 would be located closer to the sample enabling longer flight distance with the same solid angle.

The goniometer has 6 individual motorized axis (X-Y-Z, horizontal and vertical rotations and azimuthal tilt). Normally only two (Z and vertical rotation) of them are used. By rotating the vertical axis, the sample angle relative to the floor level (and the incident beam) can be changed and the sample can also be rotated towards the load lock for a sample change. By the Z-axis movement upper or lower sample can be selected from the two positions of the sample holder (see Fig. 3.3).
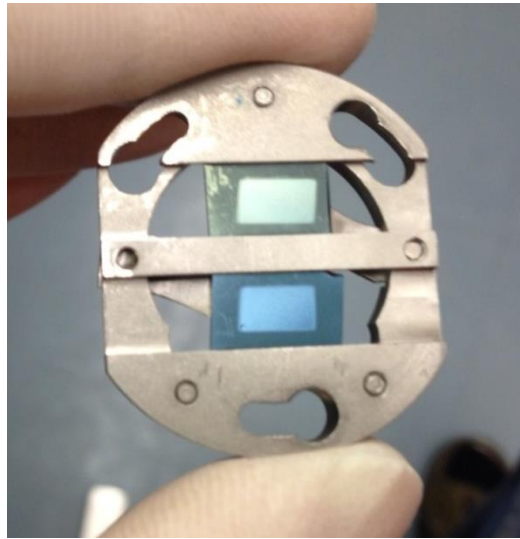
Figure 3.3: Two position sample holder for the ToF-ERDA. The slot height is 7 mm, and the beam spot area in this particular measurement has been 6.5 mm × 4.5 mm. The ion beam induced damage to the films is clearly visible.

3.2   Timing gate construction and the grid structure

The timing signal in the timing gate is generated by the secondary electrons multiplied by and MCP plate and collected from an underlying anode. These secondary electrons are created in the carbon foil from which they are emitted by the traversing ion. To suppress the unwanted events that are created by the scattered particles outside the detector solid angle or other particles flying towards the ToF-E telescope tube, two particle suppressors (metal plates with an aperture) are mounted before the first timing gate (see Fig. 3.2). The first suppressor is located inside the chamber and its opening (ϕ = 11 mm, Ω = 7.7 msr) and the size of the second suppressor (ϕ = 7 mm, Ω = 0.59 msr) are matched so that only wanted particles can pass through to the timing gates from the sample direction. Second suppressor, also shown in the Fig. 3.4, defines the solid angle for the first timing gate. Overall, the solid angle of the ToF-E telescope is limited by the T2 foil holder as the implanted silicon detector used as an energy detector has an active diameter close to 22 mm.
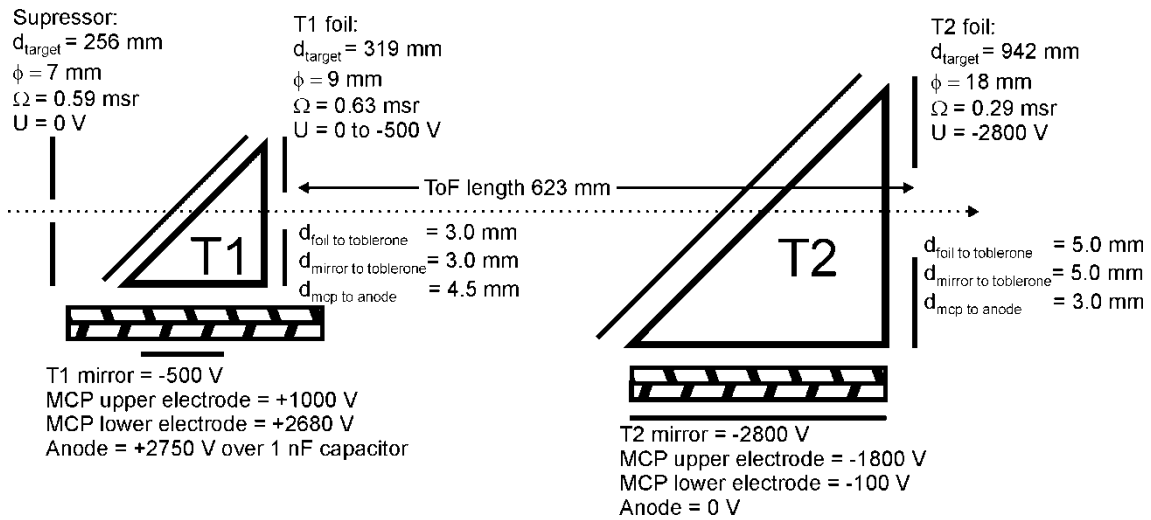
Supressor:
d_{target} = 256 mm
ϕ = 7 mm
Ω = 0.59 msr
U = 0 V

T1 foil:
d_{target} = 319 mm
ϕ = 9 mm
Ω = 0.63 msr
U = 0 to -500 V

T2 foil:
d_{target} = 942 mm
ϕ = 18 mm
Ω = 0.29 msr
U = -2800 V

ToF length 623 mm

T1

T2

$d_{foil\ to\ toblerone}$ = 3.0 mm
$d_{mirror\ to\ toblerone}$ = 3.0 mm
$d_{mcp\ to\ anode}$ = 4.5 mm

$d_{foil\ to\ toblerone}$ = 5.0 mm
$d_{mirror\ to\ toblerone}$ = 5.0 mm
$d_{mcp\ to\ anode}$ = 3.0 mm

T1 mirror = -500 V
MCP upper electrode = +1000 V
MCP lower electrode = +2680 V
Anode = +2750 V over 1 nF capacitor

T2 mirror = -2800 V
MCP upper electrode = -1800 V
MCP lower electrode = -100 V
Anode = 0 V

Figure 3.4: ToF-telescope dimensions, measures and nominal operation voltages.

Both timing gates have the same large active diameter (> 40 mm) MCPs with 12 μm pore size and d/L ratio of 1:40. Supplier of the MCPs was Tectra Gmbh [44]. Original metal anodes of the factory-made, resistively matched MCP stacks were replaced to ones made out of printed circuit boards (PCB) with patterned anode structures. Both detectors are made to fit ϕ 98 mm DN100CF T-piece. Connecting DN100CF flange has welded SHV connectors, but O-ring sealed double sided SMA-SMA connector. High voltage parts, such as the MCP stack, toblerone, foil and mirror are insulated using PEEK (polymer). Main differences in the T1 and T2 timing detectors are their physical size and the voltages as can be seen from figures 3.4 and 3.5. The T1 carbon foil can be grounded to avoid the tandem effect.

Originally there was an idea to use both the forward and backward emitted electrons of the T1 carbon foil. Backward emitted electrons, as in T2, having smaller energy spread [45], would have been used to create the timing signal. For the T1 the idea of using the forward emitted electrons was to record the position information by using the same large diameter MCP but having a separate position sensitive anode. This configuration was afterwards discarded as the timing signal was believed to be degraded by the position pulse hitting the MCP and coupling its signal to the timing anode too. The T1 timing gate, however, had all other parts ready except the position sensitive anode, including the extended distance modification from the toblerone to the MCP as can be seen from the Fig. 3.5 a). With this T1, but using only the backward emitted electrons, the first ToF-ERDA measurements were performed in Jyväskylä. When the ToF-ERDA chamber was vented after operating about one year the anode and voltage connections were modified to accommodate the anode at the high voltage and foil at the ground potential as described in Fig. 3.4 for the T1.
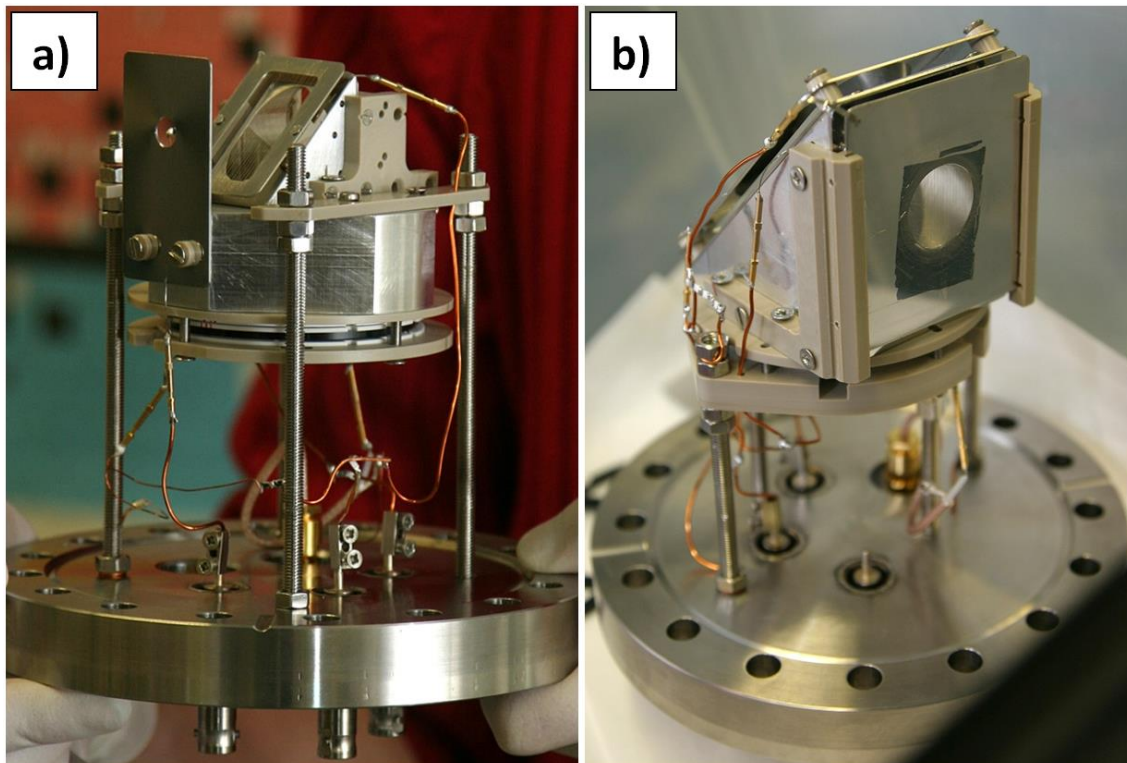
Figure 3.5: Timing gates of the first operational ToF-ERDA setup in Jyväskylä. a) T1 timing gate with forward emitted electron option not installed. b) T2 timing gate with ϕ 18 mm, 10 µg/cm² carbon foil in place.

The grid structure of the timing gates was adopted from the similar carbon foil time pick-up detectors made by Vladimir Lyapin earlier for the nuclear physics experiments in the Accelerator Laboratory. Spot welded grids were made out of 25 µm thick gold plated tungsten wire and 1.0 mm wire-to-wire spacing was chosen as this combination was proven to be feasible and well performing in the similar timing detectors. However, an error by the author was made when selecting the wire material. Without prior knowledge to the subject, 25 µm thick pure gold wire was initially ordered and used to make the first grids. Although possibly having smoother surfaces, gold wires were considerably harder to spot weld without breaking them than the gold plated tungsten wires used for the later grid versions.

Au plated W wires were ordered from Luma-Metal [46]. Grade of the wire was *"Treatment before plating: Etched"* which in practice was also the cheapest one. Later, also thinner wires down to 5 µm have been tested for the spot welding process. From these tests 10 µm diameter wire was selected to be the thinnest practical wire diameter to be handled manually and to be used in the future 0.5 mm wire-to-wire spaced grids (see more on chapter 4.1 for different wire-to-wire spacing).

The spot welding of the wires to the frame was performed using a 110 µF capacitor releasing the charge by a fast mercury switch to electroweld the wires

to the supporting frame. The welding energy was adjusted by a potentiometer adjusting the capacitor voltage up to maximum voltage of 30 V. The sharpened arc welding tip that we have been using has been normal welding tungsten from bigger machines. See figure 3.6 for the visualization of the process and a completed grid.
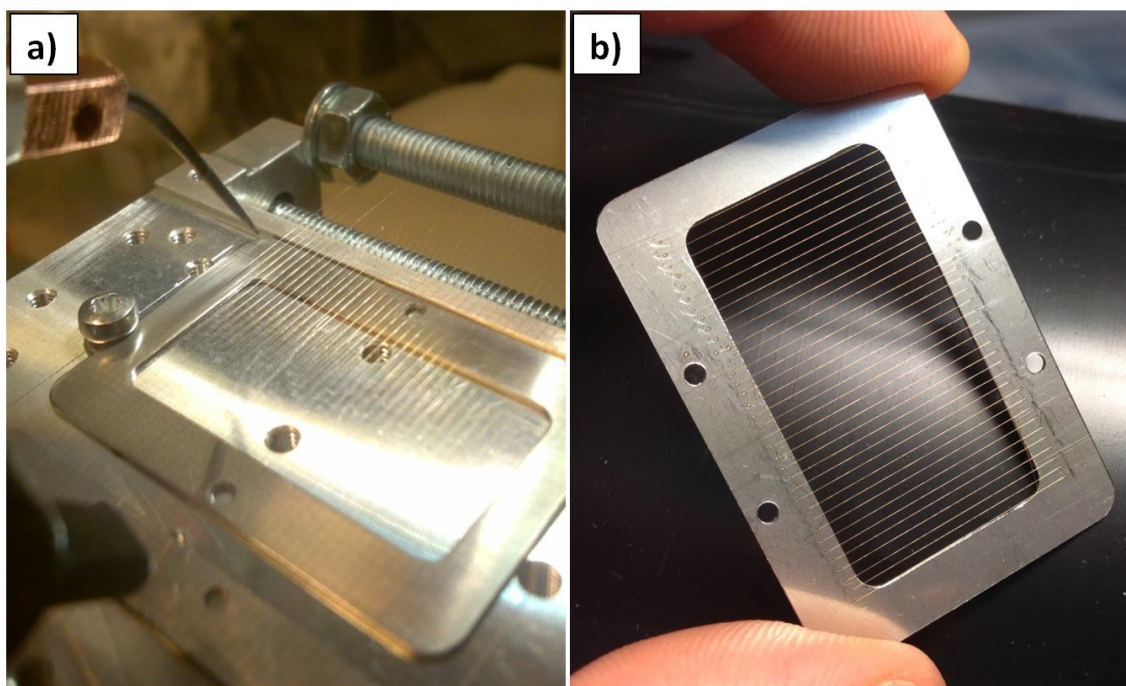

Figure 3.6: a) Point welding jig for the wire grid. Wire (20 µm in the figure) is being first wound around the jig where the pitch is determined by the pitch of the threads in both ends. Next, each wire is point welded from both ends to the frame holding the final grid structure. b) A completed grid with clean point welds for the T1 detector. Note the vertical wires, where electrons keep their 1D position better for the possible kinematic correction option (see also Fig. 4.1 for electron position information).

3.3   Energy detector

The energy detector mainly used during this thesis work was a traditional implanted silicon detector. Detectors from the both major suppliers, Ortec and Canberra, were tested without noticeable difference in the performance. The detector active area was 450 mm² and it was mounted directly (a few mm) after the T2 foil to improve the time stamping accuracy. Biggest drawback of using a solid state detector was its poor energy resolution for (low energy) heavy ions. In practice this meant that from a thin film only a single element heavier than Si could analyzed. Later, a gas ionization detector with a thin SiN window was installed which had superior energy resolution for heavy elements. This detector was taken in permanent use in the beginning of year 2013. The work with

gas ionization detector is carried out by Jaakko Julin and will be presented later his PhD thesis.

3.4 Electronics and data acquisition

Conventional analogue electronics was used for signal amplification and discrimination for two timing detectors and for an energy detector. For the energy detector, an Ortec 142 preamplifier was coupled to a shaping amplifier and further connected to an ADC (analogue to digital converter) unit. For the timing detectors, after several tests a Phillips Scientific 776 amplifier with a gain of 10, bandwidth from DC to 275 MHz and with RMS noise of 25 μV was proven to be the best choice for the fast signal pre-amplification. Amplified timing signals were fed to an Ortec 935 constant fraction discriminator (CFD) giving logical start and stop pulses to a TDC (time to digital converter) unit.

The combined ADC+TDC unit was a FAST ComTec dual TADC 7072T with a constant ADC conversion time of 500 ns. Both channels had 13 bit conversion length. The smallest 50 ns timing window width combined with the manufacturer specified resolution of 4.1 channels results in about 25 ps timing resolution. In practice, for the 500 ns timing window required in typical ToF-ERDA measurements, the timing resolution of the TADC is limited to about 250 ps.

Data retrieval from the Fast TADC was realized by modern FPGA module (National Instruments PXI-7811R-FPGA), which was also used to generate time stamps for the recorded events. The time stamping resolution is determined by the 40 MHz (equal to 25 ns) signal clock of the FPGA unit, although it was later discovered that the TADC unit could not provide data completely independently of its amplitude/length. In practice, the minimum coincidence window width was 4×25 ns for the ToF and the E signals. In typical measurements the coincidence window width was typically 12×25 ns = 300 ns.

The time stamping of each detected event allows for off-line search of the coincident events from the ASCII file, typically ~300 MB created during an hour long measurement. This permitted to optimize the coincidence window to reduce background events as discussed in more details in chapter 3.5.3.

3.5 Performance figures of the Jyväskylä setup

In this sub-chapter basic performance figures are given for the ToF-ERDA telescope and the combined data-acquisition system. These figures of merit include for example the ToF detection efficiency, the ToF resolution and the back-

ground level in the ToF-E histograms. Together these figures describe well the actual performance of the ToF-ERDA system used for the thin film analysis. [I]

The consideration of the resolution of the energy detector is left out from this discussion as for the conventional solid state silicon detector, high masses with low kinetic energy result in poor performance, as already stated above. A comparison of resolution characteristics of the solid state silicon detector and the gas ionization detector can be found from Ref. [18].

3.5.1 Detection efficiency

The probability of detecting all the ions that pass through the timing gates is not 100 % as it is for the energy detector. This is due to the smaller stopping force of lighter, higher velocity particles, namely elements lighter than carbon. Other factors affecting the detection efficiency are related to the secondary electron emission probability from the carbon foil (also independently from the stopping force), electron transport from the carbon foil to the MCP, MCP open area and its detection efficiency and the signal readout from the anode.

In Fig. 3.7 the detection efficiencies for H, He, Li and C are plotted. Comparison for the similar ToF-ERDA system at IMEC, Belgium is also shown. For carbon and heavier elements we have essentially 100 % detection efficiency, but when elemental analysis is performed for lighter elements, the reduced detection efficiency needs to be taken into account.

In our system, we have tested an additional 1 nm thick Al_2O_3-layer on the emission side of the carbon foil at the T1. The Al_2O_3-layer was grown by atomic layer deposition (ALD) [47] on top of the carbon foil while it was still on the glass substrate. The Al_2O_3 coating had a clear effect to the detection efficiency of hydrogen, the element most difficult one to detect (see Fig. 3.7 b). Same method was later tried to apply for the T2 foil also but no successful lift-off could be performed for the larger foil. It was suspected that the ALD process temperature was too high and the carbon foils sent for the process to Aalto University got stuck to the substrate. In the future, when similar ALD tool is available in house in Jyväskylä this technique can be optimized for better success rate.

We have also measured the detection efficiency curves of our MCPs for 3 MeV He ions which were scattered from a thin target. It can be seen from the Fig. 3.8 that the electron energy has no practical effect to the detection efficiency when the accelerating potential is increased above 200 V. However, increasing the potential difference between the MCP electrodes increases the detection efficiency significantly up to 1600 V where efficiency starts to saturate.
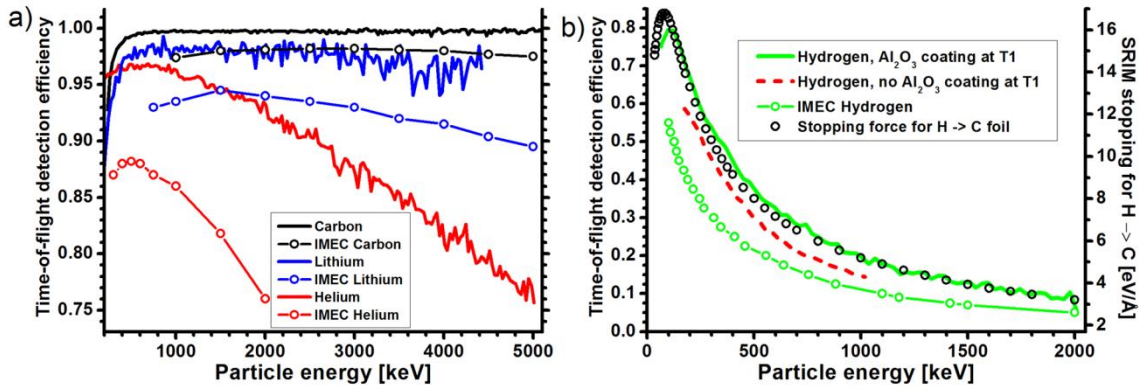
Figure 3.7: Energy dependence of detection efficiency for different ions. In a) the detection efficiencies for He, Li and C are shown together with efficiencies for another ToF-ERD system [16]. For carbon our detection efficiency is better than 99.5 %. The carbon ions which are not detected result from events with overlapping flight time (count rate dependent effect). The foils are practically pin hole free resulting negligible contribution to the detection efficiencies. In b) the detection efficiency curve for the hydrogen is shown together with SRIM stopping data for hydrogen. Even though only the first timing gate has the Al_2O_3 coating, the hydrogen detection efficiencies are clearly better for energies below 1 MeV.
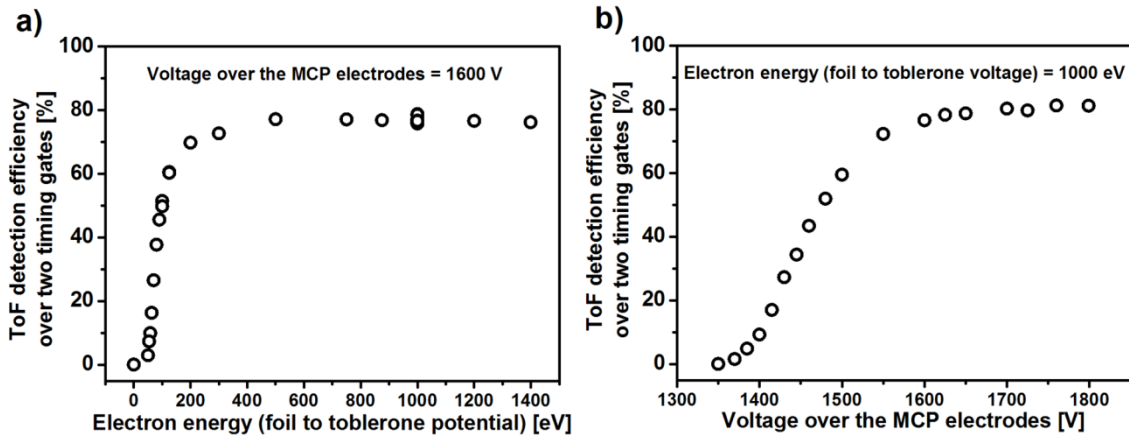

Figure 3.8: Detection efficiency of the ToF detector as a function of a) electron energy and b) MCP voltage. Measurements were made using 3 MeV He ion beam scattered from a thin target over two timing gates in a coincident mode with the energy detector, for which the efficiency was expected to be 100 %. No Al_2O_3 coating was used in the timing gate foils. a) Electron energy has very little influence to the detection efficiency when electron energy is above 200 eV. b) Increasing the MCP voltage increases the detection efficiency, although minor saturation starts at 1600 V.

3.5.2   Timing detector resolution

The kinematic spread is usually the dominant factor limiting the energy and the depth resolution close to the surface in ToF-ERD measurements. For a detector with a very small solid angle or if the kinematic spread can be corrected, the timing resolution becomes dominating effect. Although deeper in the sample

energy straggling and multiple scattering induced spreading [35] overruns the kinematic and ToF resolution induced spreading, a good timing resolution is still critical in the separation of different masses in the ToF-E histograms.

Measured timing signals and energy resolutions calculated from the ToF data are presented in the figures 3.9 and 3.10. The signals from both MCP anodes (Fig. 3.9) have rise-time of about 1 ns while T2 is slightly faster. T1 has a anode at HV and the signal is read through a 1 nF capacitor. It would be possible to improve the risetime by matched conical shaped anodes with correct terminations but the benefit for our ToF measurement system would be limited as long as the the timing resolution is limited by the TDC. This is already discussed in chapter 3.4 and can be observed in the upper sub-figure of Fig. 3.10, where the relative energy resolution becomes constant value only at high energies. Other effects than timing resolution clearly degrade the energy resolution for lower energies, indicating, for example, straggling and multiple scattering, both in the T1 carbon foil and in the thin Au scatterer used in the measurement.
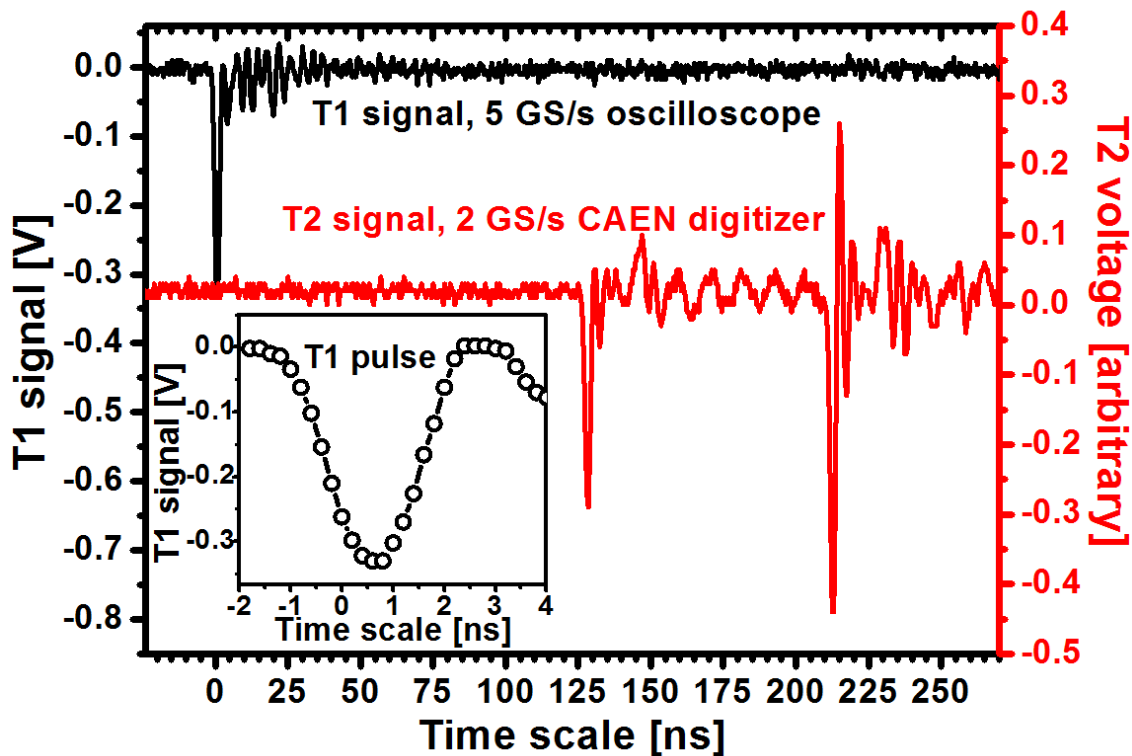

Figure 3.9: MCP signals from T1 and T2 detectors representing the start and stop events, respectively. These signals originate from different events but represent average-signals from the two timing gates. T1 signal has generally been somewhat weaker, but having also less oscillations, whereas T2 signals show strong constant oscillation or 'ringing' after the main pulse. For T2 there are actually two different events and possibly a wrong ToF-event as a result. The insert shows a magnification of the T1 main pulse.

Data for the Fig. 3.10 was measured by scattering the primary beam from a thin Au film, nominally 1 nm or 0.3 nm thick, on top of Si substrate. Thinner target was used for heavier ions. Later, after long series of experiments, the electron beam evaporated Au film was found to have non-homogenous thickness. This and the straggling and the multiple scattering in the T1 foil was believed to cause the heavier Cl to have a poorer resolution. The insert in Fig. 3.10 shows the best recorded ToF -resolution of close to 150 ps, for 4.8 MeV He whereas the trend data at 4.8 MeV He has about 200 ps (40 keV) resolution. Difference of these 4.8 MeV He values partly relate to the thicker Au scatterer used in the measurement series but the degradation of the timing foils which were in use over period of one year between the measurements cannot be excluded.
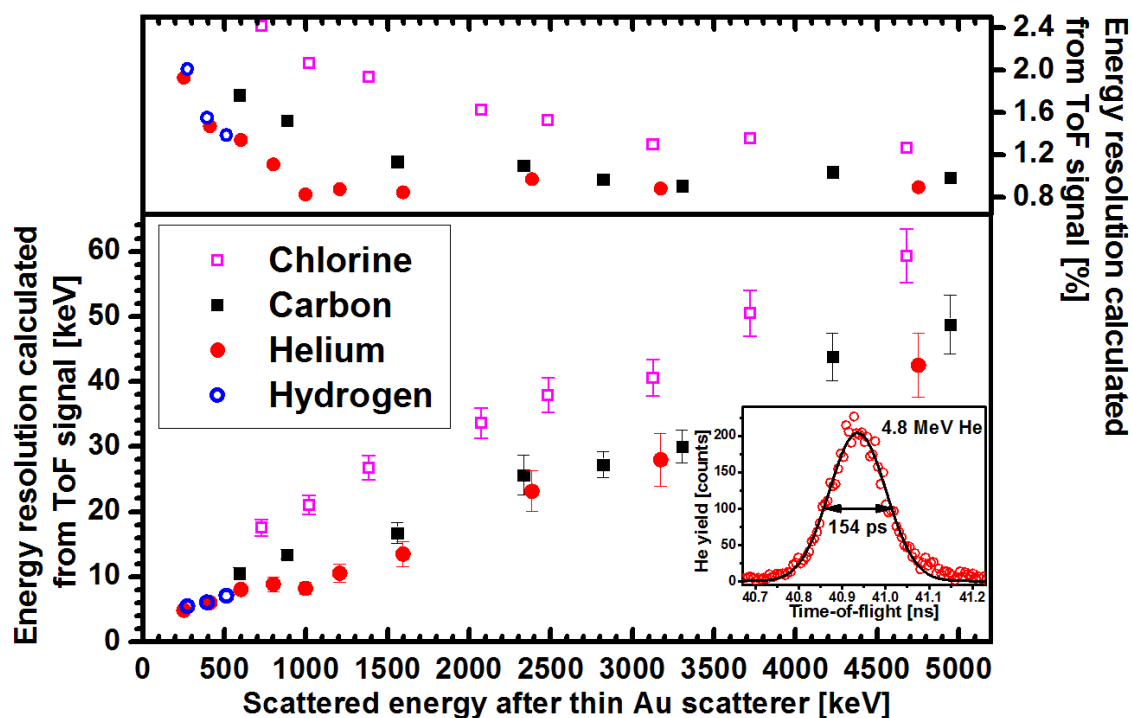

Figure 3.10: Energy resolution calculated from the ToF signal for different ions and energies. The measured resolution is defined as a Gaussian fit (FWHM) for the time-of-flight spectrum of ions scattered from a thin (few Å) Au film on Si. The relative energy resolution of the time-of-flight detector approaches ~0.9 % for all ions at higher energies. The insert shows the best recorded ToF-resolution of 154 ps, for 4.8 MeV He whereas the trend data for 4.8 MeV He has about 200 ps (40 keV) resolution. Different Au scatterer was used in the latter measurements and this is believed to explain the resolution difference.

3.5.3   Measurement background

The data acquisition of the Jyväskylä ToF-ERDA system was partly adopted from our nuclear physics groups where time stamping of all events is in active use. The time stamp accuracy of 25 ns and the free choice of the position and the length of the coincidence window allowed to reduce the background events as can be seen from the Fig. 3.11 where all events are visible. In ToF-ERDA the

background events, in general, mostly relate to the high count rates when wrong start or stop signals are generated. For example a wrong stop signal would occur in analogue signal chain in Fig 3.9 if the first peak of T2 signal is assumed to be false/background noise. Timestamp difference -histogram in the Fig. 3.11 shows how the ToF and E coincidence events have distinguishable peak at 3 µs where all true coincidences can be found. The clear peak is because of the short distance from the T2, which is the stop detector, to the energy detector. If the timing system would be wired so that start would come from T2 to reduce the number of false starts and T1 with higher count rate would act as a stop detector, a much broader coincidence window would occur and the background suppression would be much less efficient.

By being able to select the true coincidences more precisely, the background is reduced and the detection limit for different elements becomes lower. Areal densities below 5×10^{14} at. cm^{-2} have been measured for a few different cases (Al, Ge) with several samples from the surface region of the bulk films (Si/TiO$_2$, Si, respectively). For the case of hydrogen impurities, concentrations of 5–7×10^{15} at. cm^{-2} at the surface have also been quantitatively measured and analyzed (see more in chapter 5.3, Fig. 5.12).
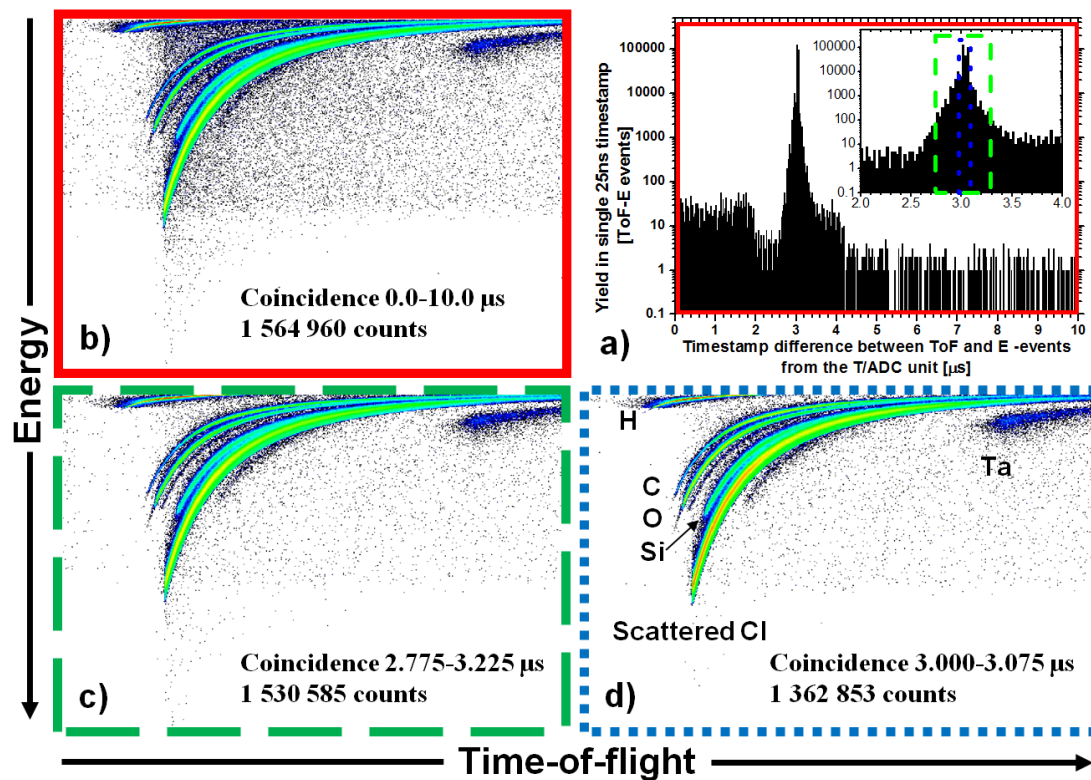
Figure 3.11: Effect of the coincidence window width to the ToF-E background. Sample was a bulk Ta metal sheet containing impurities, measured with 10 MeV $^{35}Cl^{5+}$. Histogram in a) shows a sharp peak at 3 µs position which indicates that most of the true ToF-E-coincidence events come with a constant time difference. All the coincident events with shorter than 10 µs time difference are presented in the b) ToF-E histogram (red rectangle). Shorter coincidence selections c) with green dashed (main ToF-E coincidence peak) and d) blue dotted (sharp, only 75 ns coincidence window) show clearly the reduced number of background events at.

4 IMPROVEMENT OF TIME-OF-FLIGHT DETECTOR

Time-of-flight detector composes of two individual detector units that create a start and a stop signal and with known detector distance from where the particle velocity can be calculated. In this chapter the electron transportation from the carbon foil to the MCP in a single time pick-up detector is discussed. Explanation to the halos observed around the light elemental isobars is also given. Effects concerning both timing gates, such as often mentioned tandem effect [6,16,20,26,41,43] and bending of ion flight paths for the light ions that depend on the two timing gate voltages and orientations are also discussed.

4.1 Single carbon foil time pick-up detector

A timing detector based on the Busch et al. [2] design has five basic components. These are 1: Carbon foil from which electrons are emitted, 2: Toblerone-part which creates a field free region for electrons, 3: Electrostatic mirror to bend the path of the electrons by 90 degrees, 4; MCP usually in a Chevron stack for electron multiplication and 5: An anode from which the signal is read. All of these different components have usually also different potentials applied to them (see Fig. 3.4, for example). This design enables very fast starts and stops for the ions that pass through the detectors and also the detection of even a single electron emitted from the carbon foil. [II]

4.1.1 Electron emission and transportation from the foil to the MCP

The number of electron emitted from the carbon foil is strongly dependent of the stopping force of the ion, see for example Fig. 3.7 b), but different coatings such as Al_2O_3 [I] or LiF [4] can clearly enhance the secondary electron emission yield. The electron yield is also a function of the thickness of the carbon foil (for thicknesses < 10 μg cm^{-2}) [45] and very thin DLC films used as a carbon foils [4,48] most likely will have degraded electron emission yields if additional coating is not applied. Other impurities on the carbon foil surface can also have a noticeable effect to the electron emission yield compared to a sputter cleaned carbon foil [45]. The origin of these impurities can be, for example, the lift-off process when carbon foil is lifted from water to its holder.

From the point of view of the electron transportation from the foil to the MCP, both the electron emission angle and the emission energy [45] are important. As these two cannot be controlled, the timing gate design should take these factors into consideration.

In this study the electron emission and the toblerone/mirror-grid parameters have been varied in the SimION [49] simulations where T2 timing gate was used as a model. SimION is a finite-element code for 3D-modelling of electromagnetic fields and for ray-tracing of ions in EM fields. In Fig. 4.1 only the applied voltages and wire-to-wire spacing (and mirror distance) is varied. Fig. 4.1 a), b) and c) shows that 1 mm wire-to-wire spacing is sufficient to keep the electrons still relative well together within the toblerone part. However, for 3 mm wire-to-wire spacing shown in Fig. 4.1 c) where mirror is also closer, both the field free region of the toblerone and the uniform mirror potential fail. In this particular case some of the electrons can even escape from the mirror potential as mirror grid is too close to toblerone-side grid compared to the electric field uniformity and the field strength between mirror wires that they are able to create. From the same Fig. 4.1 c) it can also be seen, when comparing to Fig. 4.1 a) and b), that the smaller the wire-to-wire spacing is, the less the electrons are angularly spread right after the first accelerating grid. This is due to the improved field free region in the toblerone and more straight equipotential lines at the grid position.

The other toblerone-grid on the mirror side has similar importance when considering the 90 degree turn of the electrons. It should also be able to create a uniform equipotential line at the grid plane and to prevent the mirror field penetrating to the field free region. As seen later in Fig. 4.2 c), the mirror wire-to-wire spacing is not critical as long as it can create a uniform equipotential line close to the toblerone side mirror grid.

The difference of the mirror potential e.g. 2 kV and the acceleration potential, e.g. 1 kV, is an important factor in the electron flight time spread. This potential difference affects also to the position spread, although the position spread is more affected by the uniformity of the toblerone-part field free region (see position spreads in Fig. 4.1 a), b) and c), for example). In Fig. 4.1 d), e) and f) only the mirror field and the acceleration potential differences are changed. Green dots representing 200 ps time intervals show clearly that in Fig. 4.1 d) the time spread at MCP top electrode is larger than in the case of Fig. 4.1 e) and f). This is because the electrons spend longer time in the mirror volume in Fig. 4.1 d) where electrons penetrate about half-way between the mirror grids. Whereas in Fig. 4.1 e) and f), despite the different trajectories due to the emission angle, the arrival times of the electrons to the MCP are very same. Reason for this is that in the Fig. 4.1 e) and f) electrons make their 90 degree turn much closer to the toblerone-side mirror grid and spend less time in the mirror volume. This turning point cannot be, however, brought infinitely closer to toblerone-side's mirror grid because of the individual wire potentials will ultimately induce similar effect than is presented in Fig. 4.1 c).
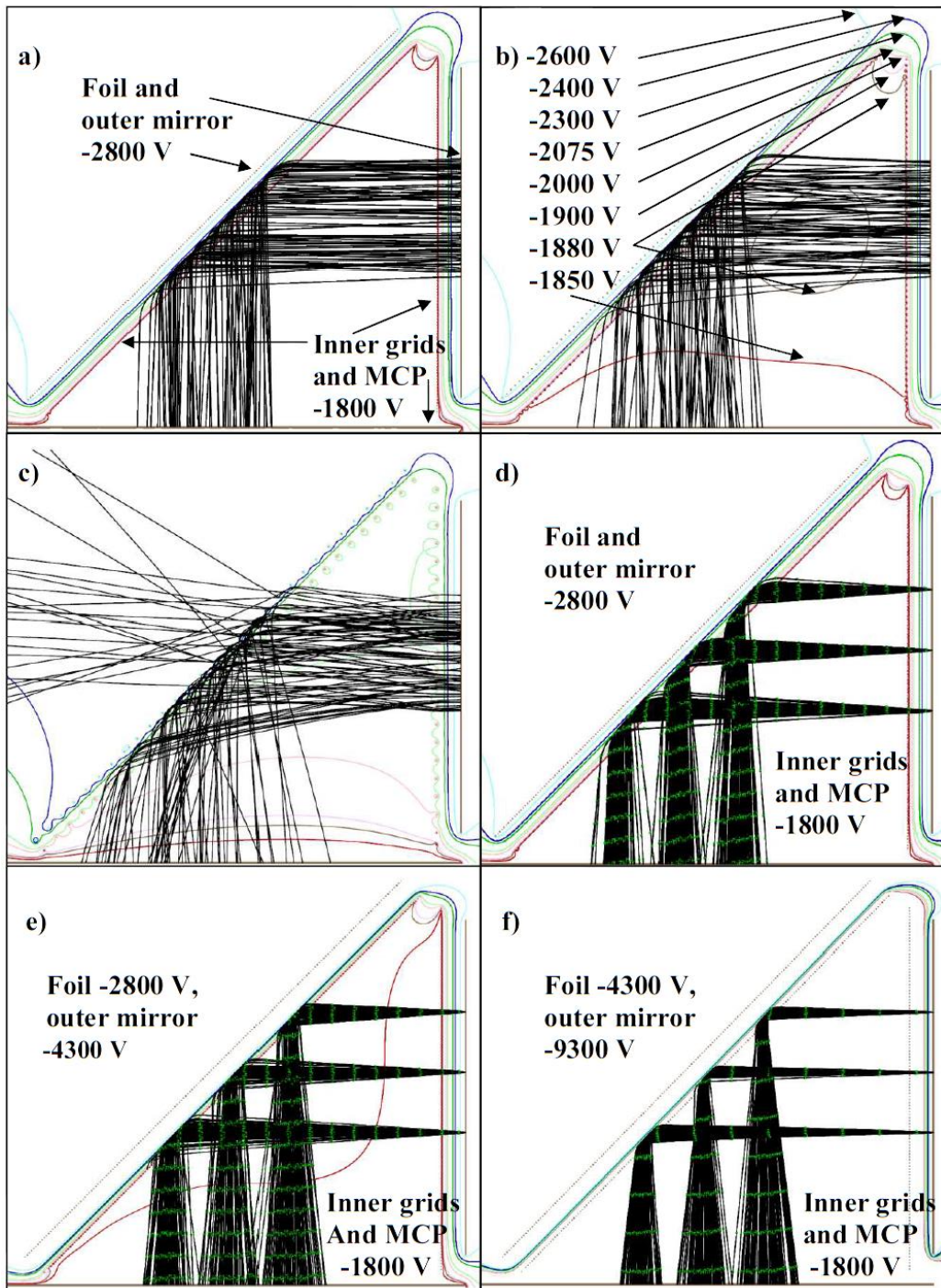
Figure 4.1: Electron trajectory simulations made with SIMION program for the T2 timing gate with different wire-to-wire spacings and applied voltages. In a), b) and c) the wire-to-wire spacings are 0.5 mm, 1 mm and 3 mm, respectively, where b) represents the experimental configuration in Jyväskylä. In c) the outer mirror grid is brought 1/3 closer to the inner mirror grid from the original perpendicular distance of 5.0 mm. In d), e) and f) the accelerating foil potential and the outer mirror potential has been changed for the 0.5 mm wire-to-wire spacing –case. The (green) markers on the black electron paths indicate 200 ps time intervals. In these simulations, all electrons emitted from the foil have initial energy of (4 ± 6) eV with uniform distribution of ± 40 degree perpendicular to the foil surface.

Simulation results for different electron flight times and spreads are collected in the Fig. 4.2. Here electron emission parameters, emission angle and energy, are changed with the different T2 timing gate parameters. From the Fig. 4.2 it can be concluded that higher acceleration voltage (foil and mirror) reduces the average electron flight time and spread equally but the worst case events having high electron emission angle and energy induce the largest spread to the electron flight times.

There exists an optimum mirror voltage for certain acceleration voltage (and wire-to-wire spacing). This can be seen from the Fig. 4.2 b) where a clear minimum in the electron flight time spread exists at about -4500 V mirror grid voltage (acceleration potential being -2800 V and toblerone -1800 V). The mirror potential should thus be about 2.5 - 3 times higher than the accelerating potential for small wire-to-wire spacing. The maximum applicable mirror grid voltage increases when approaching the ideal grid. It must be noted, though, that the actual fields depend also on the device structure and its dimensions. The same phenomen as demonstrated in Fig. 4.1 d), e) and f) and in Fig. 4.2 b) is seen with the red and also green dotted curves in the figures 4.2 c) and d). The actual distance or even wire-to-wire spacing of the outer mirror grid does is not critical. However, the equipotential lines the outer mirror grid is able to create near the toblerone-part mirror grid, needs to be straight and not to follow the spherical electric field lines of the individual wires. If this distance where electrons bend 90 degrees towards the MCP is brought closer to the toblerone-part mirror grid, the electron flight time spread does get smaller.

Therefore, to conclude this sub-chapter it can be noted that judging from the Figs. 4.1 and 4.2, the 0.5 mm wire-to-wire spacing is recommended for the toblerone grids, whereas one can save some effort on the mirror grid where clearly wider spacing works equally well. However, the mirror grid equipotential line position does depend on the wire-to-wire spacing but a potential of 2-3 times higher at the mirror grid than in the acceleration from the foil should be used. If using 10 μm wire diameter, as discussed earlier in the chapter 3.2, one can still obtain > 88.5 % optical transmission for 6 grids. However, there are some recent experimental evidence that 10 μm wires at high voltages increase background in the timing gates significantly compared to the thicker 20 or 25 μm wires. This is something to be confirmed later. In acceleration potential, shown partly in Fig. 4.1 a) one needs to do a compromise as too high voltages not only lead to practical problems, such as sparking, but also will degrade the actual ToF resolution because of the tandem effect.
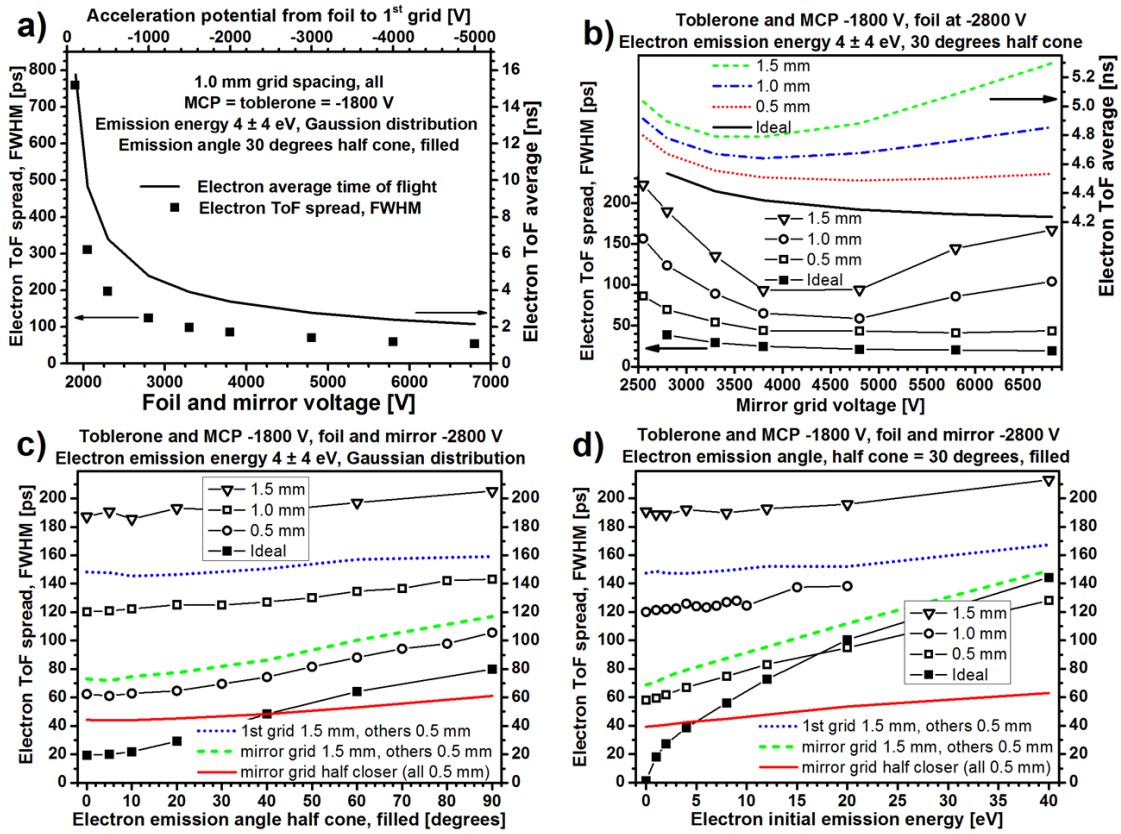
Figure 4.2: The effect of different timing gate and electron emission parameters to the electron flight time spread. a) The electron ToF spread and the electron flight times as a function of foil and mirror voltage. b) The TOF spread as a function of mirror grid potential for a fixed foil voltage. The TOF spread as a function of electron emission energy c) and emission half cone d).

4.1.2   Origin of the halo structure in the ToF-E histograms

For elements lighter than carbon, a halo structure (see Fig. 4.3) can often be seen around the curved isobar as in (see Fig. 1.2, [29] and [26]). This phenomenon was studied by means of simulations and experiments [II]. From the experimental results presented in the Fig. 4.3 it can be concluded that longer than normal electron flight times from the foil to the MCP, at both timing detectors, were causing the halo structure, i.e. extra events at longer and shorter ToFs. It was also concluded that these were single electron events as lowering the MCP voltage and therefore gain made them disappear. The smaller than average signal amplitude of these halo events was also confirmed with the fast digitizer units.
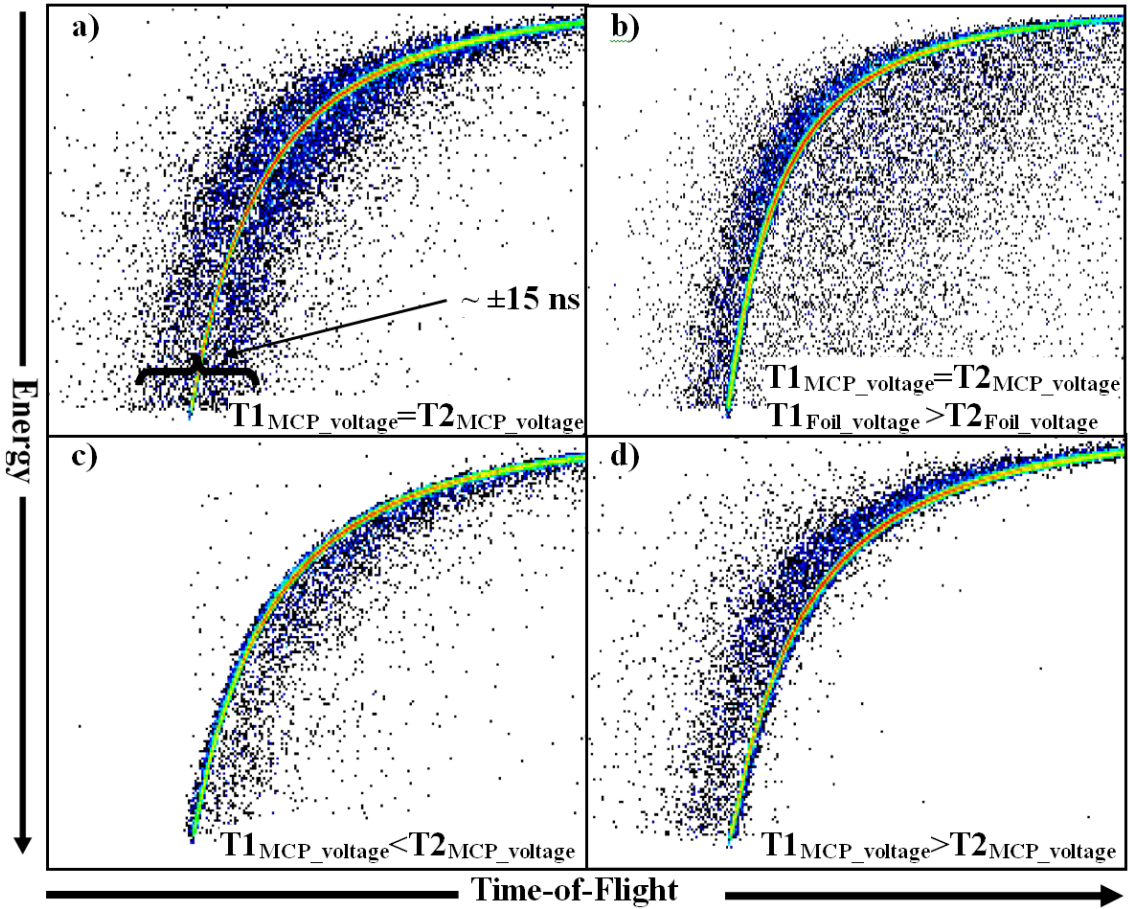
Figure 4.3: Time-of-flight−energy histogram showing the influence of the MCP voltage and foil voltage to the scattered hydrogen ion TOFs. When operating at nominal voltages for our system, hydrogen has a clear background distributing over ±15 ns from the main isobar as well as lighter background spreading further away as shown in a). In b) only the T2 foil has reduced voltage and therefore only smaller electron energies are available within the T2. In c) only T1 MCP gain has been lowered so that only multiple electron events generate detectable signals at T1 (similarly for T2 in d).

In the beginning there were two candidates for the origin of the single electron halo events: the electrons had either a) scattered from the grid wires during their flight path from the foil to the MCP, or b) backscattered from the MCP surface before entering the active MCP pore and multiplication. In order to test these two candidates, simulations with detailed grid structures needed to be done. Before running the simulations the electron backscattering probabilities from the MCP surface and wires and the MCP detection efficiency, needed to be solved especially for very low energies.

Data from CERN [50,51] was used to estimate the backscattering probability as a function of incident electron energy. These data had slightly different primary energy than our electrons (550 eV vs. our data was with 1000 eV) and the backscattering material was copper, not Ni as in MCP electrode or Au/W as in grid wires. For the MCP detection efficiency for very low energies, older data from Ref. [52], originally measured for channeltron, was used. Here also was a

problem: the efficiency data extended only down to 10 eV from where it was needed to be extrapolated to lower energies. Data from these references, which was also used in the simulations, are presented in Fig 4.4.
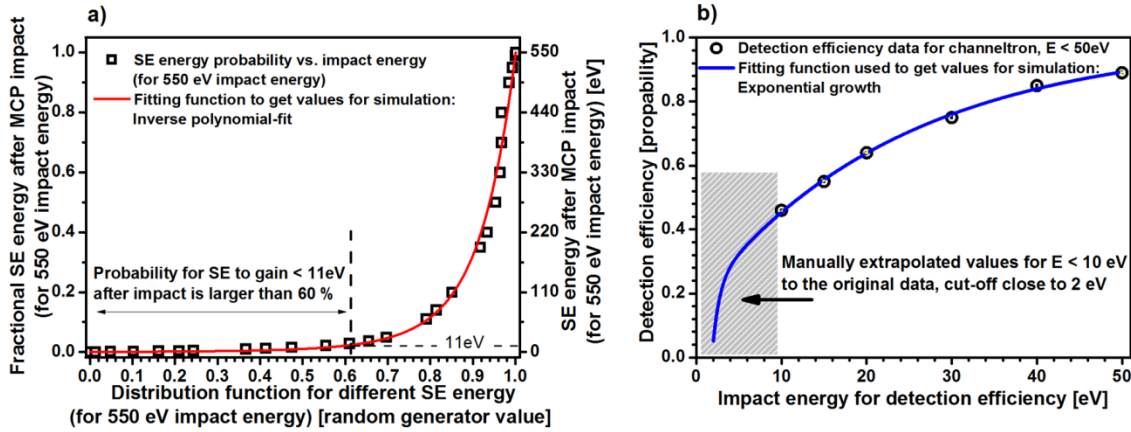

Figure 4.4: The secondary electron emission energy distribution as a distribution function (probability) and b) MCP detection efficiency vs. electron impact energy. The probability function in a) was used to calculate the energy for the emitted electron after the primary electron had hit to the wire or the MCP surface. About 60 % of these secondary electrons had less than 11 eV (= 0.02 × 550 eV) energy although small amount of the emissions occurred almost at impact energies (true backscattering events). In b) estimated values for the detection efficiency of the MCP were taken from Ref. [49] down to 10 eV and the points below the 10 eV impact energy are approximated with a cut-off value of < 2 eV. Higher than 50 eV impact energies were assumed to have constant detection efficiency (~90 %) in the simulations.

When simulations were made to calculate the electron flight times from the foil to the MCP, the probability function for backscattered energy distribution from Fig. 4.4 a) and MCP detection efficiency function from Fig. 4.4 b) were used. It was separately calculated if the electron hit only the grid wires or if it had the possibility to hit both the grid wires and the MCP surface and still backscatter from there. Only those electrons that ended up to the MCP surface after the scattering event were taken into account. The electron flight paths, including the backscatter events, were like the ones seen in the Fig. 4.5.

Experimental data, taken from the events presented in the Fig. 4.3 is shown together with the simulations in Fig. 4.6. When only the scattering events from the grid wires were taken into account, the intensity and shape of the flight time yield was different compared to the set of events which included also scattering from the MCP surface. The scattering events from the MCP surface matched well the experimental shape once the MCP detection efficiency for low energy electrons was taken into account. There exists, however, a sharp peak at 15–16 ns in the Fig. 4.6. Large portion of this peak was traced to the events where backscattered highest energy electrons make multiple wiggles in the toblerone before ending back to the MCP surface. As similar peak is missing from the experimental data, this would indicate slight over estimation of the

true backscattering yield at close to original energy, compared to the secondary (backscattered) electrons with lower energies. Also if a lower foil/grid voltage is used, longer time scale of the halo will result from the simulation, similarly as seen in experiment presented in the Fig. 4.3 b).
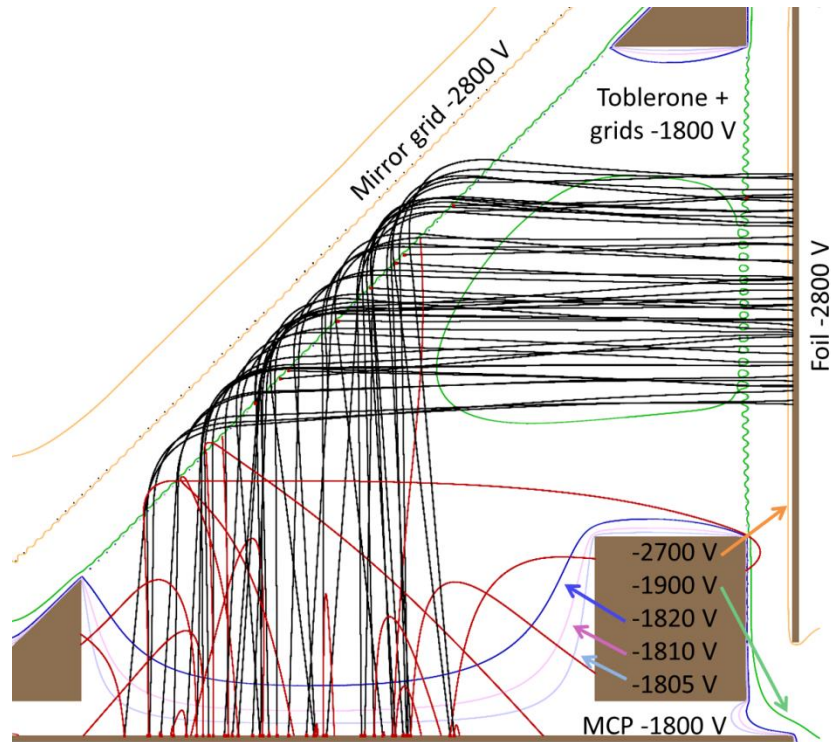

Figure 4.5: Electron paths (43) in our current T2 timing gate simulated with nominal parameters. Single secondary electron emission was set to occur due to the primary electron impact. About half of the secondary electrons (48 in total) from the MCP have too little energy to be visible in this scale. In total, 10 secondary events end up to the toblerone side mirror grid and 5 to the walls of the toblerone block, while majority of the secondary electrons from the MCP surface end up back to the MCP surface and can generate a signal.
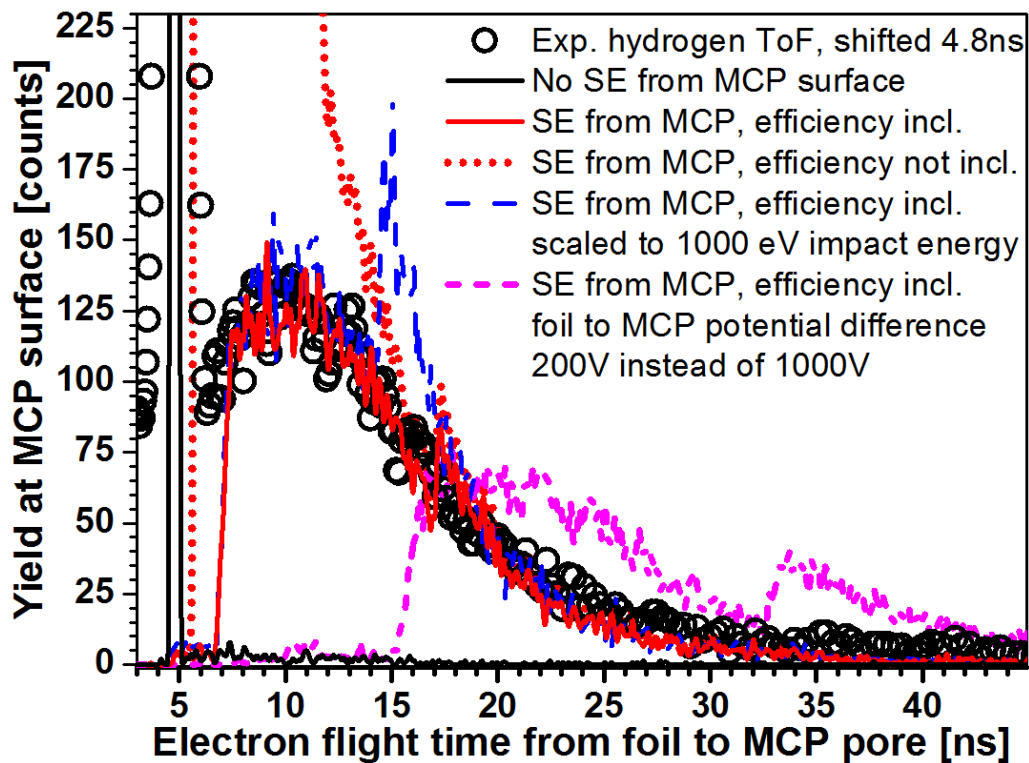
Figure 4.6 Experimental time-of-flight data from the hydrogen ions and corresponding electron flight time simulations from the carbon foil to the MCP surface in our current T2 detector. The use of 1000 eV impact energy instead of 550 eV changes very little the overall shape of the extended flight times with the exception of the shifted peak which is present at the simulations (see text). The solid black line represents the case in which scattering/secondary events only from the wire grids are considered. The dashed pink line shows the extended electron flight times for reduced foil and mirror potentials. In the experimental data the main peak (at 4.8 ns) has about 75 % of all events detected.

When the experimental evidence and the results of the simulations are combined, it can be concluded that the halo events in the ToF-E histogram have origin in the single electron secondary emission at the MCP surface. These low energy electrons cannot escape from the toblerone volume and they end up to the active MCP pore after a short flight time. It would be an advantage to more effectively utilize also these single event secondary electrons and thus enhance the detection efficiency for hydrogen and other light elements. This could be done by additional electric field created by a wire grid between the MCP and the toblerone, which would 'push' the secondary electrons immediately back to the MCP surface. This would induce small time delay for these low energy secondary electrons but in some situations it could be tolerable if hydrogen or other light element detection efficiency should be as high as possible. After a heavy ion impact to the carbon foil, there will always exist some secondary electrons from the MCP surface which have longer flight times. However, for the heavy ions this is not a problem since many secondary electrons emitted from the carbon foil end up directly in the MCP active pore and create a signal at the correct time.

4.2   Time-of-flight detector composing of a two individual time detector units

In the previous subchapter optimized design of a single timing gate was discussed. Next we extend the simulations and experiments to ions and to the full time-of-flight detector system with start and stop detector. Two issues will be discussed: the tandem effect and the effect of electric fields to the ion flight path. [III]

4.2.1   Influence of the tandem effect to the time-of-flight of the ion

The tandem effect, first discussed in chapter 2.2.4 and example reference being [6], is often said centralize to the foil of the first timing gate. The energetic ions traversing in the foil first undergoes a process to reach the charge state equilibrium (see Refs. [21,53] for example), after which the average charge state could be for example *+1.3* for He ions for certain energy. This means that all charge states (total of three here) of He ion are present after the foil but the average of these would be something between *1+* and *2+* states and the neutral charge state *0+* would be a minority. As ions with different charge states emerge out of the T1 carbon foil, they gain, or lose, the amount of energy equivalent to the voltage of the foil times the charge state of the ion. Thus, a random process causes ions to exit from the T1 foil with different energies, even they would have the same kinetic energy before the foil. This ultimately results as a spread in the time-of-flight distributions, degradation of the ToF resolution and hence also the depth resolution.

The bigger picture is, however, more complicated, as one needs to take into account also the charge state distribution before the foil, the timing gate orientation, other voltages of the both timing gates and their parameters [III]. The charge state probability distribution of the ions exiting from the T1 foil, however, is in fact the same as before the foil because it is a velocity dependent distribution [21] and the ion energy loss in the foil is minimal.

Four different timing gate orientations were simulated to test if the timing gate orientation have any impact to the tandem effect. The different variations are shown schematically in Fig. 4.7. In the simulations the same timing gate sizes for T1 and T2 and same foil-to-foil distance were used as in the existing ToF-ERD configuration. Typical simulation run consisted of three equal-energy ions having a mass of 4 u (representing He^0, He^{1+}, He^{2+}), incoming from the sample direction. Because of the T1 foil voltage, these three ions then had 3 different energies when they reached the T1 foil position. At the T1 foil position total of 9 (3×3) ions were then emitted towards the T2. Finally, the time-of-flight was recorded for all of these 9 ions between the T1 and T2 foils.

Ion beam direction

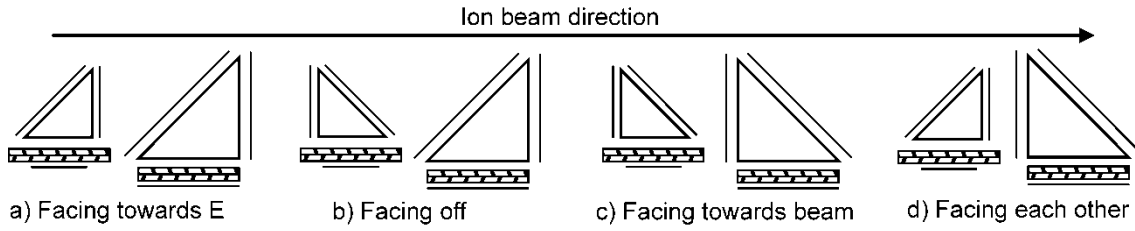a) Facing towards E   b) Facing off   c) Facing towards beam   d) Facing each other

Figure 4.7: Different timing gate orientations. In all simulations the distance from foil-to-foil was kept the same. Both timing gate carbon foils in a) face towards the E detector, in b) face off from each other, in c) face towards the beam and in d) face towards each other.

Next, the different time-of-flights, for the selected energy, were weighted according to the different charge state fractions that the simulated ions did experience during their flight (including the charge state distribution before the T1). These fractions were taken from [54] and some of the used values are tabulated in the Table 1. The nine different flight times subsequently had nine different probabilities forming distribution of more or less Gaussian profile with some average time-of-flight and spread of this value. These probabilities and distributions are illustrated in Fig. 4.8, where two different T1 voltages are compared.

Table 1: Charge state fractions for low energy He ions in a carbon foil, taken from [54]. q_{av} is the average charge state and d is the width (sigma) of the distribution.

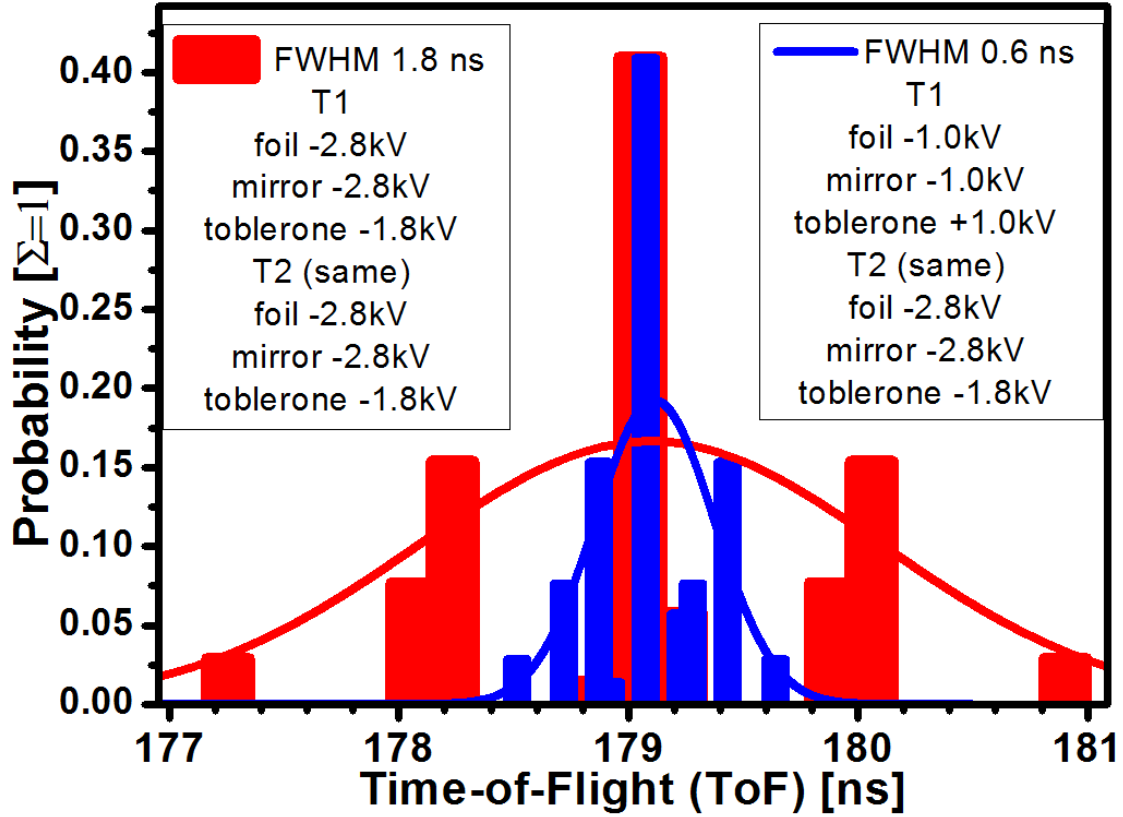| He energy	Charge state distribution			q_{av}	d
[keV]	2+	1+	0		
150	0.05	0.60	0.35	0.70	0.56
250	0.12	0.64	0.24	0.88	0.59
400	0.30	0.60	0.10	1.20	0.60
600	0.51	0.46	0.03	1.48	0.56
800	0.67	0.32	0.01	1.66	0.49

Figure: 4.8: Simulated tandem effect induced time-of-flights for monoenergetic 250 keV He ions with three different charge states. Correct 250 keV He⁰ time-of-flight is 179.23 ns. Both timing gates faced towards the energy detector. Probabilities for different charge states are taken from [54]. Fitted curves are pure Gaussian, FWHM is calculated through weighted standard deviation σ obtained directly from the data.

The highest peak in the Fig. 4.8 represents the event in which *1+* charge state ion was incoming towards the timing telescope T1 and also flying towards the T2 after T1 foil. The *1+* charge state probability thus was *0.64 × 0.64 = 0.41*. It can also be seen from the Table 1 that the spread in ToF, caused by the tandem effect, depends on the energy of the ion, which in practice governs the natural charge state probability distribution of the ions. When single charge state has high probability compared to the other charge states the spread in ToF will in practice be narrower than in the case where the charge states are distributed equally among many. This is also the situation for the high energies approaching MeV/u where all ions start to be close to fully stripped when passing through the solid foil. This is the case for close to 100 % of He^{2+} ions at the energies of above 2 MeV [54].

Both the time difference to the correct ToF and the simulated ToF resolution degradation [FWHM] are presented for all timing gate orientations in Fig. 4.9. Here a 150 keV energy for different incoming He charge states was used.

From the same Fig. 4.9, it can be noted that there is no difference between the different timing gate orientations in the tandem effect. However, the best orientation, where time difference is the smallest to the correct ToF (see Fig. 4.9), is the one where carbon foils face towards each other (Fig. 4.7 d). This time difference, however, has little meaning in practice as the differences are very small compared to the correct ToF.
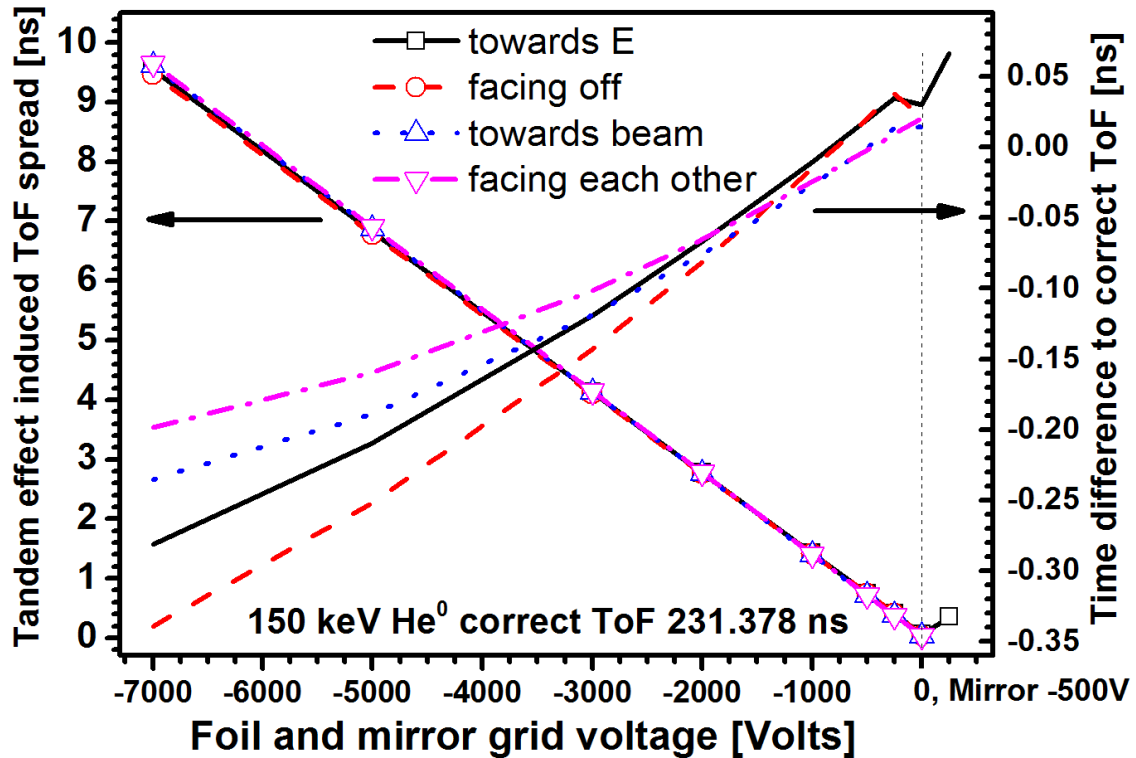

Figure 4.9: Impact of the timing gate orientation to the tandem effect induced ToF spread (left y-axis) and peak position shift (right y-axis). Both timing gates had the same voltages in all configurations. Simulated ion beam was 150 keV He and toblerone-part voltage was +1000 V for both timing gates. Timing gate orientation schematics can be seen from Fig. 4.7.

Further simulations were made to determine how does the voltages in T1 and T2 change the magnitude of the tandem effect. Same 150 keV He ions were used in the Fig. 4.10 as in Fig. 4.9. The timing gate orientation was facing towards the E-detector as in Fig. 4.7 a). The constant voltages for T1 and T2 in Fig. 4.10 refer to the +1000 V toblerone and -500 V mirror and foil voltages.

As can be guessed, and also visible in Fig. 4.10, the T1 voltages have a significant impact to the tandem effect and T2 only minor. The same figure similarly shows that it is the foil voltage of T1 which has the greatest influence, and mirror and toblerone voltages have only minor importance when considering the resolution degradation (Fig. 4.10 a). For the shift with respect to correct ToF, on the other hand, both the mirror and toblerone voltages do have an impact, as

seen from the Fig. 4.10 b) but the overall impact to the ToF-ERDA results is meaningless. By having constant T1 voltages but increasing the T2 foil and mirror voltages, it also seems like it could be possible to compensate the tandem effect of T1 foil with the second timing gate voltages. This is indicated by the lines with near zero slopes in the Fig. 4.10 a) and b) where increasing T2 voltages reduces the tandem effect to almost half. This is caused by the T2 equipotential field penetrating more deep into the ToF beam tube, towards the T1, where it compensates the acceleration or deceleration of the ions after the T1 foil. In overall, however, the T1 mirror grid and toblerone and the T2 voltages have no impact to the tandem effect, if the T1 foil has high voltage. The T1 mirror and T2 voltages have significance only when T1 foil voltage is below 1000 V, as can be seen from Fig. 4.12.
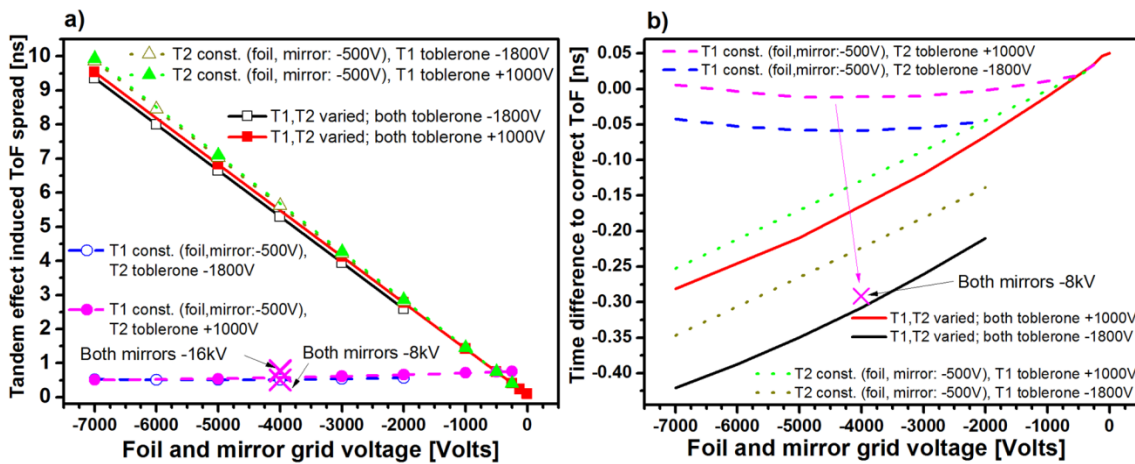

Figure 4.10: Impact of timing gate voltages to the tandem effect induced ToF spread (a) and peak position shift (b). In a) the simulated spread is given as FWHM. Simulated 150 keV He ions were used and correct ToF for He^0 is 231.378 ns. The foil in both timing gates was facing towards the energy detector. Constant voltages in a) and b) refer to +1000 V in toblerone and -500 V in mirror and foil. Crosses where both mirrors are at high voltage, -8 kV or -16 kV, refer to the situation where T1 and both mirror voltages are constant and T2 foil voltage is -4000 V and toblerone +1000 V.

When different beam energies were used in the tandem effect simulations, relatively linear resolution behavior was noticed to couple with the T1 foil voltage which finally led to formula (16) . Although the timing resolution degradation in *ns* does decrease for higher energies, the calculated energy resolution in *keV* stays relatively constant. These are shown in Fig. 4.11 a) and b), respectively. From the Figs. 4.11 b) and c) it could be interpreted that both the T1 voltage and nuclear charge Z (meaning also the number of electrons of the atom) of the ion have direct impact to the magnitude of the tandem effect. Whereas from the Fig. 4.11 d) it seems like the ion energy would have only very little impact to the magnitude of the tandem effect. After plotting these figures, an estimation of the tandem effect was created in a form of a formula

$$\Delta E_{\text{tandem effect}} = 3.33 * d * V_{\text{T1 foil}} \text{ ,} \tag{16}$$

where ΔE [keV] is the energy resolution spread in FWHM, d is the width of the charge state distribution [III] and $V_{\text{T1 foil}}$ [kV] is the T1 foil voltage in kV. The multiplier 3.33 comes from the $2.355 * \sqrt{2}$, where 2.355 is the factor to convert sigma, the value of d, to FWHM and $\sqrt{2}$ is the extra spreading caused when incoming ion charge state spread is quadratically summed with the charge state spread leaving from the T1 foil. The width d is together with q_{av} the most often measured value in the measurements determining different charge state distributions and can be found in reference data bases such as the one in Ref. [55]. This estimate (16) is also shown with the simulated data in the Fig. 4.11 b), c) and d).
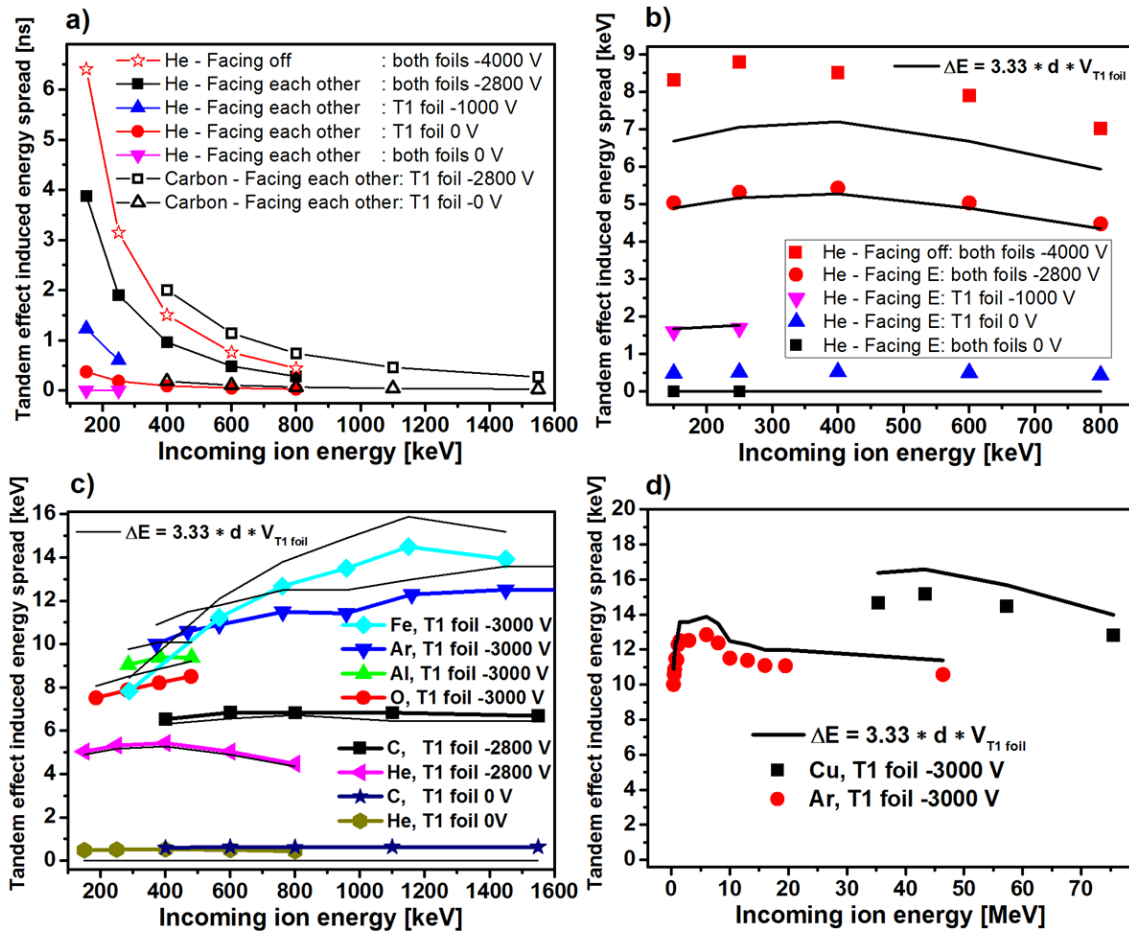
Figure 4.11: Simulated resolution degradation in nanoseconds (a) and keVs (b, c and d) due to the tandem effect for different ion masses and beam energies. The y-axis are in FWHM. Also an estimation for the tandem effect is shown in b), c) and d) as a solid line. The charge state fractions for different ions used in the simulations are taken from the following references: He [54], C [56], O [57], Al [57], Ar(< 1.5 MeV [56],> 1. 5 MeV [58]), Fe [56], Cu [59].

To see the average effect of T1 foil to the estimated resolution degradation, a 150 keV He beam was used in Fig. 4.12. These values are partly the same as in Fig. 4.9 and the same values are behind the data points of 150 keV energy in Fig. 4.11. From 0 to -1000 V T1 foil voltage, other effects and voltages also contribute to the tandem effect as seen from the Fig. 4.12. From these results, as a rule of thumb, a T1 foil voltage of 500-600 V can be said to cause the tandem effect of 1 keV to the He ions. This number compares very well to the measured values reported in [6].

Presented formula (16) for the estimation of the tandem effect shows good consistency of ~10 % to the simulated values of wide energy, ion mass and T1 voltage range. However, (16) being only a two term formula with a constant, it also clearly fails when T1 foil voltage drops below -500 V (see Fig. 4.12) where other voltages of the timing gates start to have greater influence to the passing ion.

The formula (16) does anyway give a solid number for the magnitude of the tandem effect, something what previous assumptions made for the tandem effect have not succeeded to quantitate.
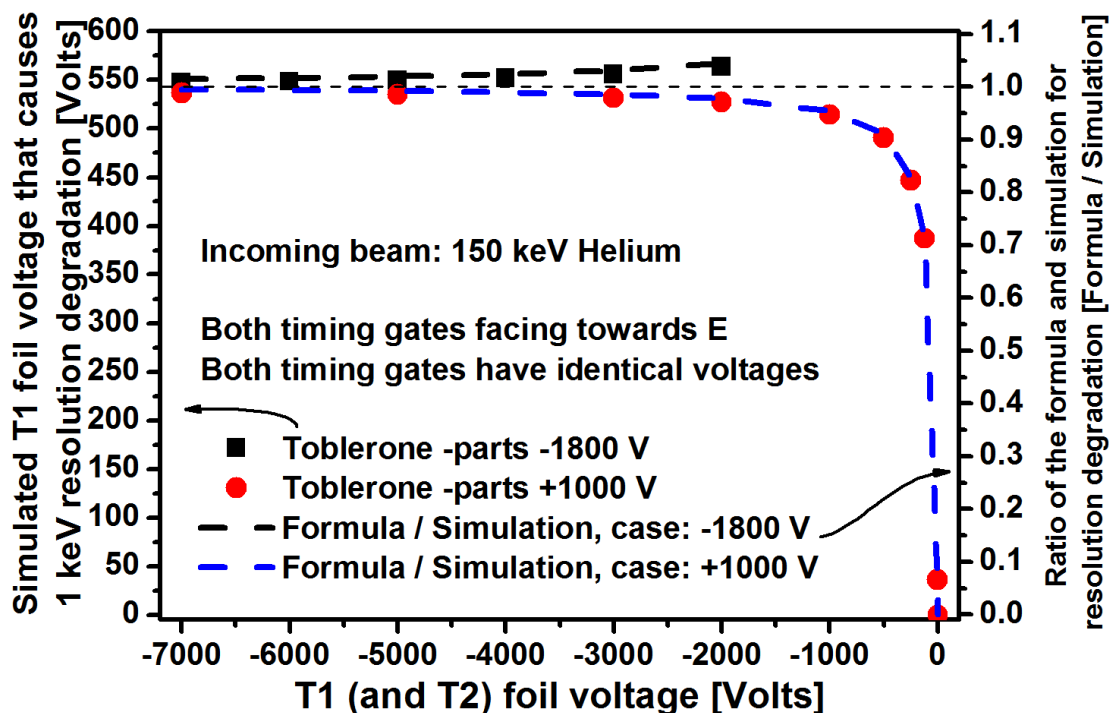

Figure 4.12: T1 foil voltage dependence and the accuracy of the formulation. Left scale: T1 foil voltage that causes 1 keV degradation to the simulated energy resolution. Right scale: a comparison between the formulation and the simulation in the T1 foil voltage range. Right scale scaled to 1.0 where T1 foil dependence is at linear region. 150 keV He beam was used with the timing gate configuration where both timing gates face towards the E detector.

4.2.2   Bending of the low energy ions in the electric fields of the timing gate

When tandem effect was simulated, it was noted that with low energy ions, the flight paths of the light ions can vary significantly, depending on the timing gate voltages. This was primarily due to the T1 mirror to toblerone potential difference. The effect was most pronounced for the hydrogen energies between 50 and 150 keV. In some situations it was seen that low energy ions could ultimately miss the T2 timing gate or the energy detector completely, because of this bending.

Lowest energy hydrogen ions having (straight or) upward trajectory in Fig. 4.13 b) would not be detected at energy detector at all. This bending of the light particles in the T1 would result a loss of hydrogen events and a falsified hydrogen concentration in a depth profile. In our case, however, this is not true as for the both front suppressors (see Figs. 3.2 and 3.4), the solid angles before the T1 are sufficiently large. This leads to the situation where hydrogen ions that

would have otherwise ended up too low in T2 are now bent upwards and generate a corresponding signal. The average number of these events equals to the amount of missing hydrogen events that have ended up too high in T2. This effect somewhat cancels the loss of events caused by the bending effect. But, if the front suppressor would limit the solid angle this correcting counter effect would be prohibited and the unwanted loss of low energy hydrogen ions would take place.

It is also worth to notice that this counter effect can in some circumstances even add hydrogen events to the spectrum at the lowest energies, if the suppressor is badly aligned and T1 has high potential difference between the mirror grid and toblerone-part. When smaller than 100 keV hydrogen events are important, the bending of the ions in the first timing gate cannot be neglected. For heavier ions with similar or higher energies, this type of bending is not significant.
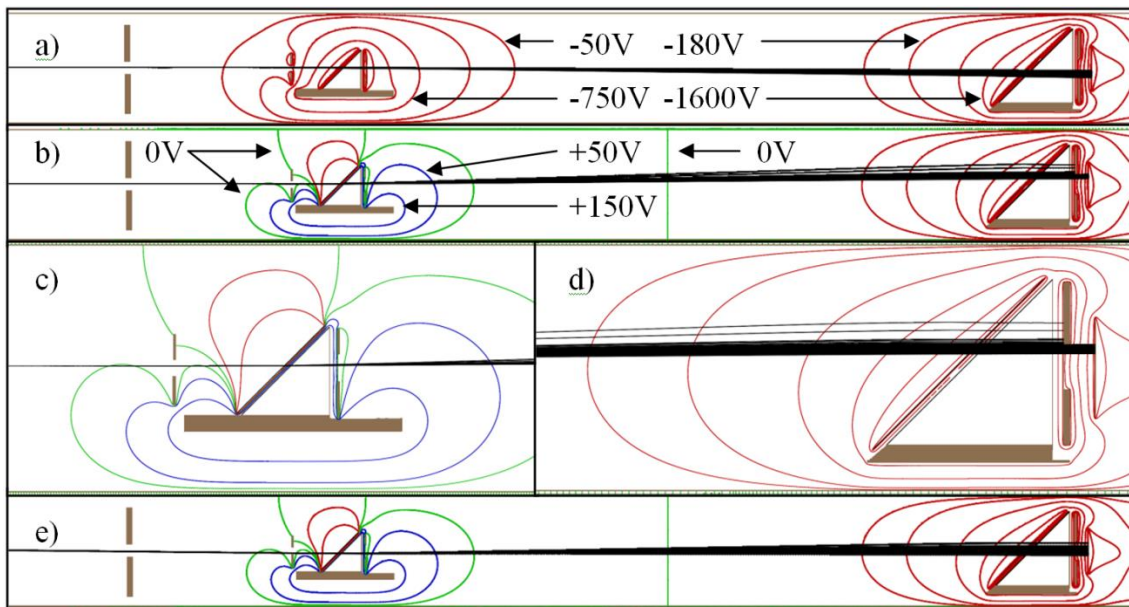

Figure 4.13: Bending of hydrogen ion trajectories in timing gates. Low energy hydrogen ion paths (initial energy 100 ± 50) keV) are simulated with SimION through the ToF-ERD spectrometer with E-detector being further right after the T2 timing gate. Red color: negative potential, green color: neutral potential and blue color: positive potential. In a) both T1 and T2 have foil and mirror voltage at -2800 V and virtually field free toblerone part at -1800 V. In the rest of the figures the T1 foil is at the ground potential, the mirror at -500 V (to repel free electrons as in the experimental setup) and the toblerone part for the T1 at +1000 V. One can see that in b) and in the close-ups of c) and d) the hydrogen paths at lowest energies will not end up to the E-detector when the foil opening at T2 is 18 mm in diameter. In e) where 1% downward declination is used for incoming hydrogen ions regarding to the straight line of sight.

To conclude the chapter 4.2 where the timing detector composing of two timing gates is discussed, it can be confirmed that the parameters affecting to

the tandem effect also affect to the bending of the ions. When considering the tandem effect the small as possible T1 foil voltage is recommended, although the tandem effect has real impact to the ToF results only energies below 1 MeV where tandem effect dE/E can be several % for high T1 foil voltages. In the case of Fig. 3.10 where for example energy resolution of 1.4 % was measured for the 500 keV He and the measurements were done with low T1 foil voltage, the contribution from the tandem effect is < 0.2 % (see also Figs. 4.11, 2.7). Timing gate orientation on the other hand has no practical influence to the magnitude of the tandem effect. The obtained results suggest also restrictions to the T1 mirror field which can bend the low energy light particles. T1 Mirror electric field strength should be kept smaller than 1500V/3 mm if for example hydrogen ions with E < 100 keV needs to be measured with similar detector system having tightly fixed solid angle.

5 ANALYSIS EXAMPLES

The ToF-ERDA tool built during this thesis work is primarily used for quantitative depth profiling of thin films. Majority of the measured samples have been related to the ALD process development of thin films like ruthenium [60], AlN [61], Al2O3/TiO$_2$ nanolaminates [IV], iridium [62], ZnO [63], silver [64], copper [65], osmium [66] or TiO$_2$ [67] to mention a few. While smallest measured areal concentrations have contained less than 1×10^{15} at. cm^{-2} implantations of specific atoms or just 1,2,3,5 ALD cycles of Al$_2$O$_3$ [68], corresponding 1-5 Å thicknesses, the thinnest actual depth profiled films have been 5 nm thick Al$_2$O$_3$ -layers on Si (see Fig. 5.1).
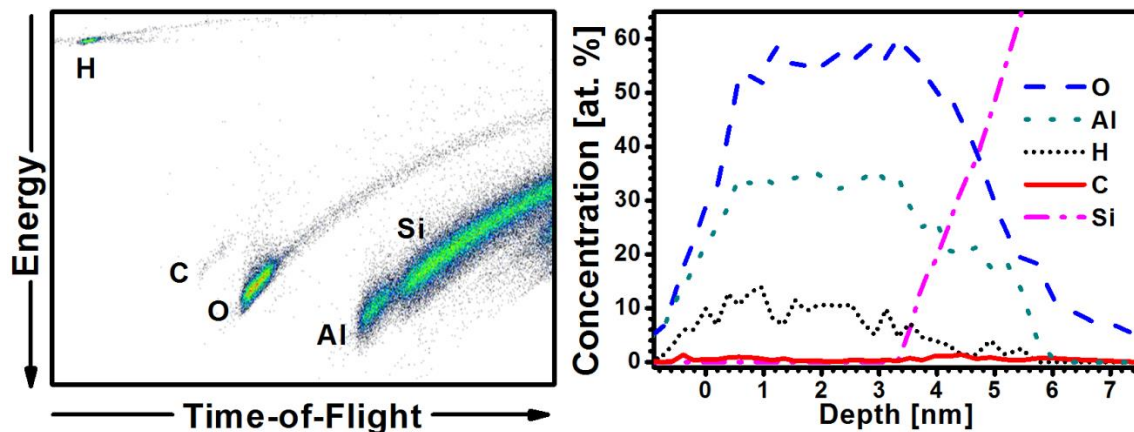

Figure 5.1: A raw ToF-E histogram (left) and depth profile (right) of 5 nm thick Al$_2$O$_3$ film on Si. No events are omitted from the shown histogram. Sample was measured with 5.1 MeV Cl^{2+} beam while tilt angle was 2.75 degrees from sample surface to the detector. Density of 3.1 g/cm³ determined by XRR was used to convert the depth profile from at. cm^{-2} to nm. Thin film was deposited by Oili Ylivaara in VTT, Finland and XRR measurement was done by Sakari Sintonen in Aalto University, Finland.

In this chapter are presented three very different demonstrations of the measurements that have been done during the past years. First one is a more traditional two-composite nanolaminate of TiO$_2$ and Al$_2$O$_3$ used to test the limits of the tool performance, second is an example from stopping force measurements and third describes a method of probing small, sub-monolayer, concentrations of Al$_2$O$_3$ on top of the TiO$_2$/Si substrate structure.

5.1   Separation of the individual nanolaminate layers

During the ALD related TEKES project, ALEBOND[2], where bonding properties of different ALD thin films were studied, Jyväskylä was a project partner and provided elemental depth profiles and elemental compositions measured with the ToF-ERD. During the project we also received several nanolaminate samples to be analyzed. These multilayered samples with well-defined individual layer thicknesses provided us a good benchmark to test our relatively new ToF-ERD tool at that time. This work has been published in [IV].

Multilayered nanolaminate samples composed of several Al_2O_3 and TiO_2 layers grown on top of each other. The substrate was always a Si wafer. The thicknesses of the individual layers were from 1 nm to 20 nm and the full thickness of the nanolaminate was kept constant, about 50 nm.
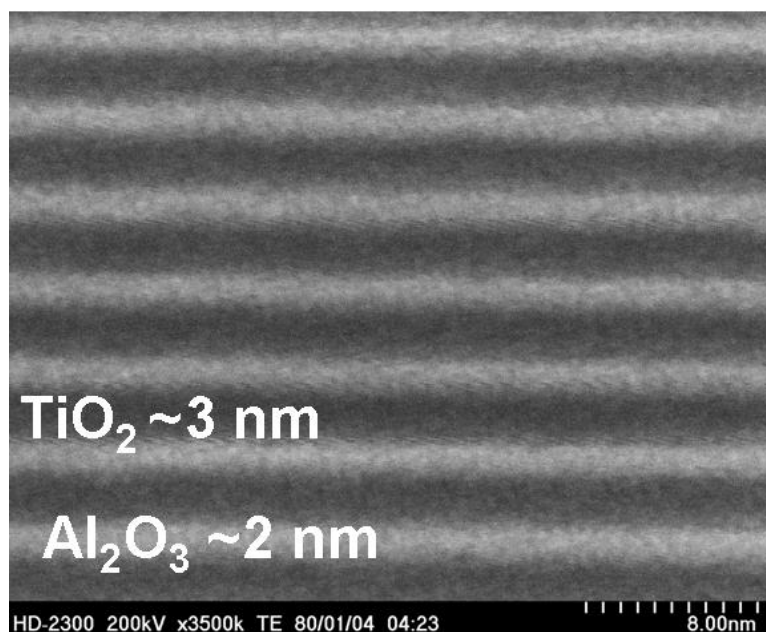

Figure 5.2: Cross sectional transmission electron microscope image of the Al_2O_3/TiO_2 nanolaminate. Similar nanolaminate structures grown by the same ALD processes were analyzed with the ToF-ERD during this study.

---

[2] Nanocoatings with tailored roughness for controlled surface bonding (ALEBOND) was a part of TEKES Functional Materials Programme (2007-2013).
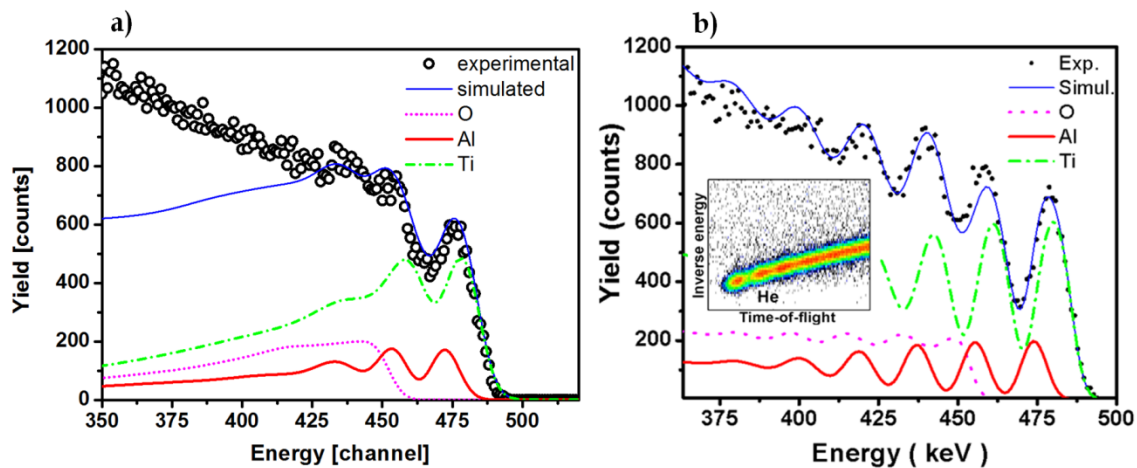
Figure 5.3: Forward scattered He spectra of a) 1 nm and b) 2 nm thick individual nano-laminate layers. Simulation fits represent SimNRA [69] simulations of assumed Al_2O_3 and TiO_2 layer thicknesses and compositions. The 1 nm layers were measured with 515 keV He beam at 3 degree angle between the surface and the ToF-E telescope. Here, only the first layers of the composite form a clear dip in the spectrum and simulation could not reproduce correctly the measured data deeper in the sample (as seen in a) without unrealistic tweaking of the parameters. b) In the 2 nm case, measured with same energy as a) but with 6 degree angle between the surface and the ToF-E telescope, up to 7-9 individual layers could be matched with SimNRA simulation to the experimental data.

In the Fig. 5.2 is presented a cross-section of a similar nanolaminate structure than those depth profiled and characterized in the [IV]. Fig. 5.2 shows clearly separated individual Al_2O_3 and TiO_2 layers.

Nanolaminate samples were measured with both light and heavy ions with the ToF-ERDA spectrometer. He and C ions were used to test the resolution limits of the ToF-spectrometer with thinnest samples whereas heavier ions such as Cl were used to depth profile the atomic concentrations in the film. In the measurements shown in Figs. 5.3 and 5.4 only the scattered primary beam was used in the analysis. Measurements with the low energy He and C beams proved that if the light impurities are not of interest, and the major components of the film are known, scattered beam can be used to depth profile and analyze the composition of the nanolaminate structures very effectively.

For the 5 nm thick layers, more conventional ToF-ERDA method was also able to resolve individual layers throughout the film (see Fig. 5.5). If compared with Fig. 5.4, the same sample measured with scattered C, the lighter projectile retains the depth resolution better deeper in the sample than the recoiled Al or scattered [35]Cl beam used to probe the Ti in the case of Fig. 5.5 b). Although the elemental composition is more difficult to obtain using the scattered C, the better depth resolution for heavier elements can be beneficial in studies when resolving between the mixed and the separate laminate layers in important, for example.
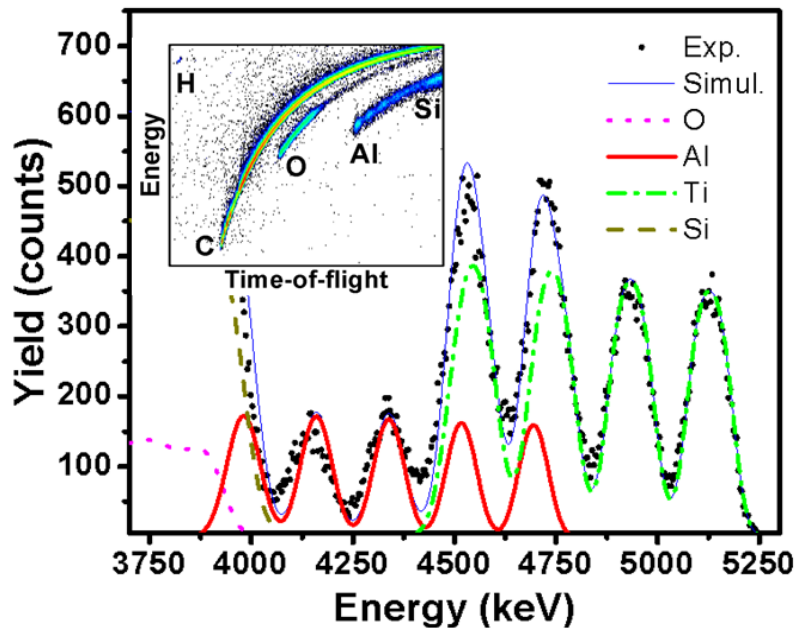
Figure 5.4: Forward scattered ^{12}C spectrum of the 5 nm thick layers. SimNRA simulation can reproduce very well the detected ^{12}C yield of the measured with the 6 MeV $^{12}C^{3+}$ at 6 degree angle from sample surface to beam.
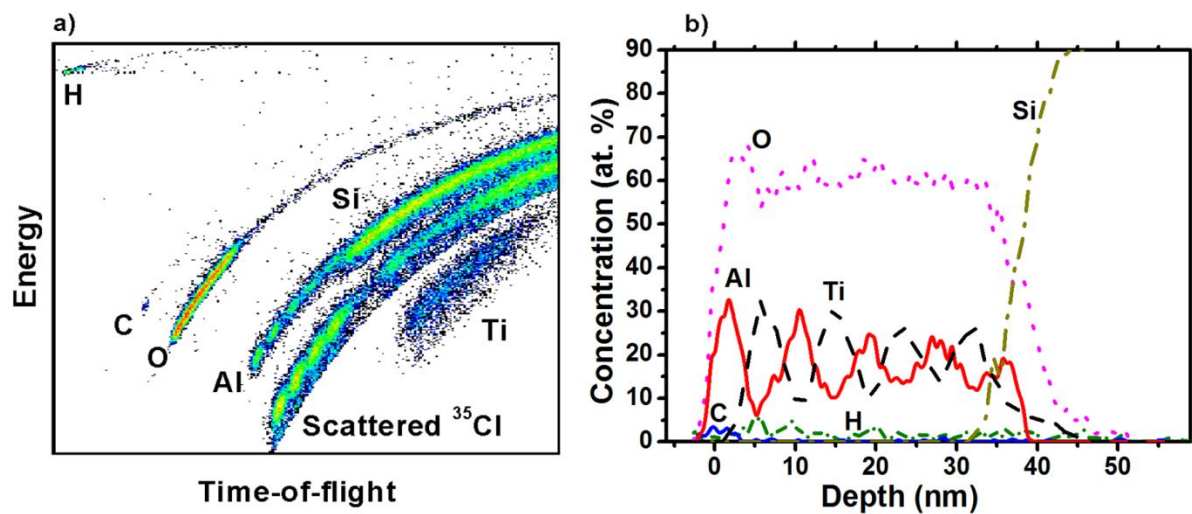

Figure 5.5: a) The raw ToF-E histogram and b) the depth profile of the 5 nm thick nanolaminate layers measured with the 9.9 MeV $^{35}Cl^{5+}$ at 6 degree angle from sample surface to the detector. Depth profile is normalized to 100 % for every depth and density of 3.5 $g\ cm^{-3}$ was used to convert $at.\ cm^{-2}$ to nm.

In the nanolaminates with 5 times 10 nm layers, as shown in Fig. 5.6, the layes are separated throughout the film. It must be noted, though, that the last 10 nm layer (5 nm on Fig. 5.5) of Al (in Al_2O_3) on top of the Si substrate needs already a sophisticated guess, when the Al events are selected from the histogram for depth profiling. Another important curiosity is the comparison of H-profile in Fig. 5.6 versus the Fig. 3 in the [IV]. In [IV] Fig. 3 an error had occurred to the author when using Finlandia analysis software. Due to a wrong

sample tilt angle (sample to detector - angle (6°) was used in input field of the program instead of beam to sample -angle (35°)) the depth profile for hydrogen ends already in the middle of the film which is not the case in reality as shown in Fig. 5.6. This type of dramatic error in the sample angle, however, does not always cause a radical change in the actual depth profile. The only major difference is for the hydrogen because the hydrogen coming long way out from the sample loses still very little energy compared to other elements in the film. Stopping force difference, due to tilt angle, can also be seen in the histogram of Fig. 5.6 a) where the isobar of H is significantly shorter than the ones for the rest of the elements in the film. If the tilt angle would have been shallow, i.e. the heavier ion beam with greater stopping force would have travelled longer path in the film, the length of the H isobar should be more comparable to other elements in these energies. If high resolution depth profiling of hydrogen is critical, this is the way to tilt the sample then.
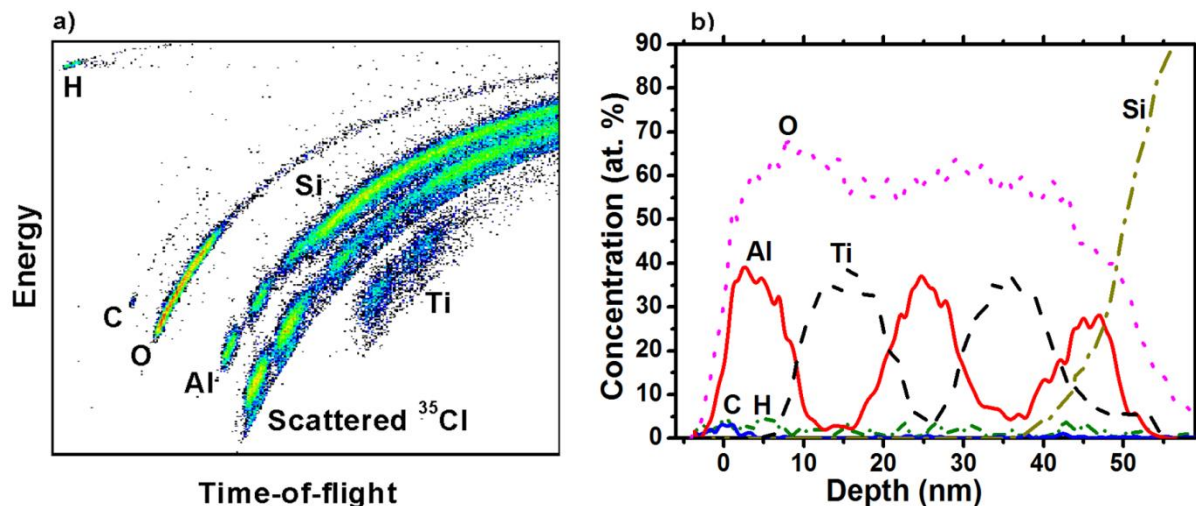

Figure 5.6: a) The raw ToF-E histogram and b) the depth profile of the 10 nm thick layers measured with the 9.9 MeV $^{35}Cl^{5+}$ at 6 degrees from sample surface to the detector. Depth profile is normalized to 100 % for every depth and density of 3.5 g cm^{-3} was used to convert at. cm^{-2} to nm.

5.2   Energy loss measurement

In a small part of an IAEA coordinated research project (CRP)[3] energy losses of heavy ions in advanced engineering materials were measured with the Jyväskylä ToF-ERDA spectrometer. The aim of this project was to "address identified shortcomings and limitations in the utilization of heavy ions through the delivery of better analytical tools with a higher degree of reliability, accuracy, and user confidence, thereby enabling an expansion in the range of problems addressable and solvable". In short, also stopping forces for heavy ions in 100 nm thick Si_3N_4 window and different materials deposited on top of it were to be measured in European facilities having ion beam analysis tools.

Sample holder addition shown in Fig. 5.7 was constructed to enable stopping force measurements with the obtained Si_3N_4 windows and other materials deposited on top of similar windows. This sample holder allowed one data point per single energy to be measured with two consecutive measurements: with and without the Si_3N_4 window. Primary beam from the accelerator was scattered from a very thin Au film on top of a Si substrate to obtain a sharp peak with the ToF detector [70] . Energy of the incident ion beam was based on the generating volt meter (GVM) measuring the accelerator terminal voltage, and the GVM calibrated against the 3036±2 keV $^{16}O(\alpha,\alpha)^{16}O$ resonance with two different terminal voltages before the measurements.
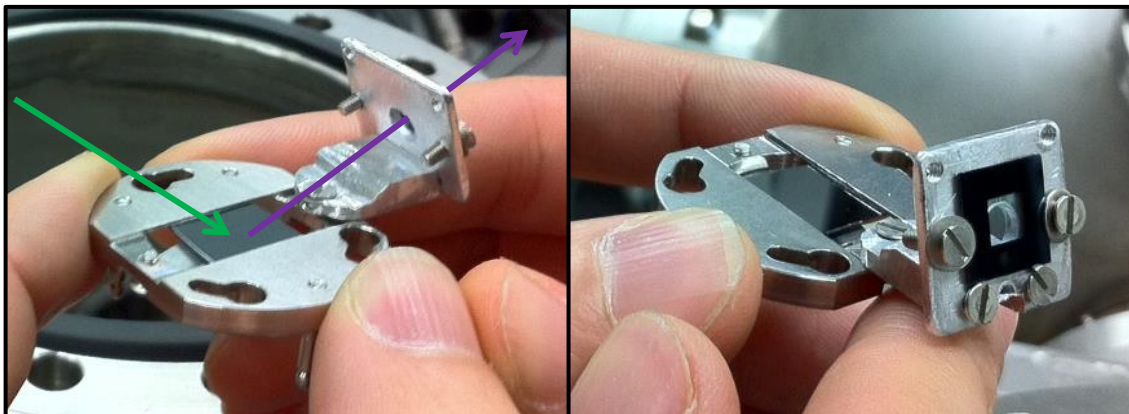

Figure 5.7: Sample holder for stopping force measurements with the ToF-ERDA spectrometer. Incident ions (green arrow) hit the thin Au film on a Si substrate to scatter (violet arrow) towards the telescope. Sample holder can be tilted to an angle where scattered ions pass through the 100 nm thin Si_3N_4 window before entering the ToF-E telescope and hence lose some energy compared to the measurement with without the window.

---

[3] IAEA CRP code: F11013
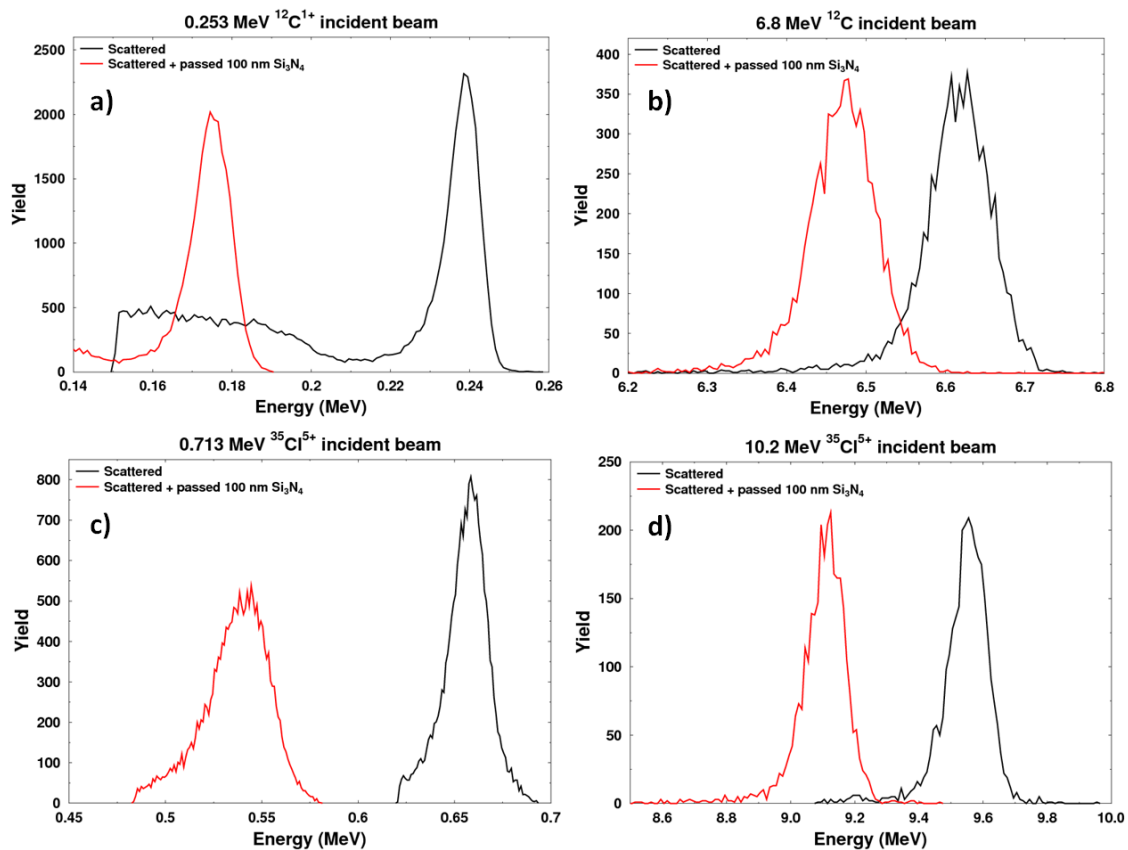 Improvement of the Reliability and Accuracy of Heavy Ion Beam Nuclear Analytical
 Techniques

Figure 5.8: Four example measurements of the energy loss in 100 nm Si₃N₄. The spectra in a) and b) are measured with low (0.253 MeV) and high (6.8 MeV) energy ^{12}C ions, respectively, and c) and d) are similar measurements made with ^{35}Cl incident beam.

Stopping force measurements were based on the detected peak position energy difference with and without the Si_3N_4 window as shown in Fig. 5.8. While the individual energy point takes two consecutive measurements the center position of the peak, and the shift, is easy to determine as large statistics to the peak can be collected in a relatively short time period.

The determined stopping force of the Si_3N_4 and Al_2O_3 for ^{12}C and ^{35}Cl ions is presented in Fig. 5.9. Experimental values show 10-20 % deviation from the SRIM [71] values, higher values for Si_3N_4 and lower values for Al_2O_3. These deviations for insulating nitrides and oxides (and other ceramics) were also expected and the measuring more accurate experimental values was one of the original aim of this IAEA project, to which also the Jyväskylä data was handed in to be published as a TECDOC document.
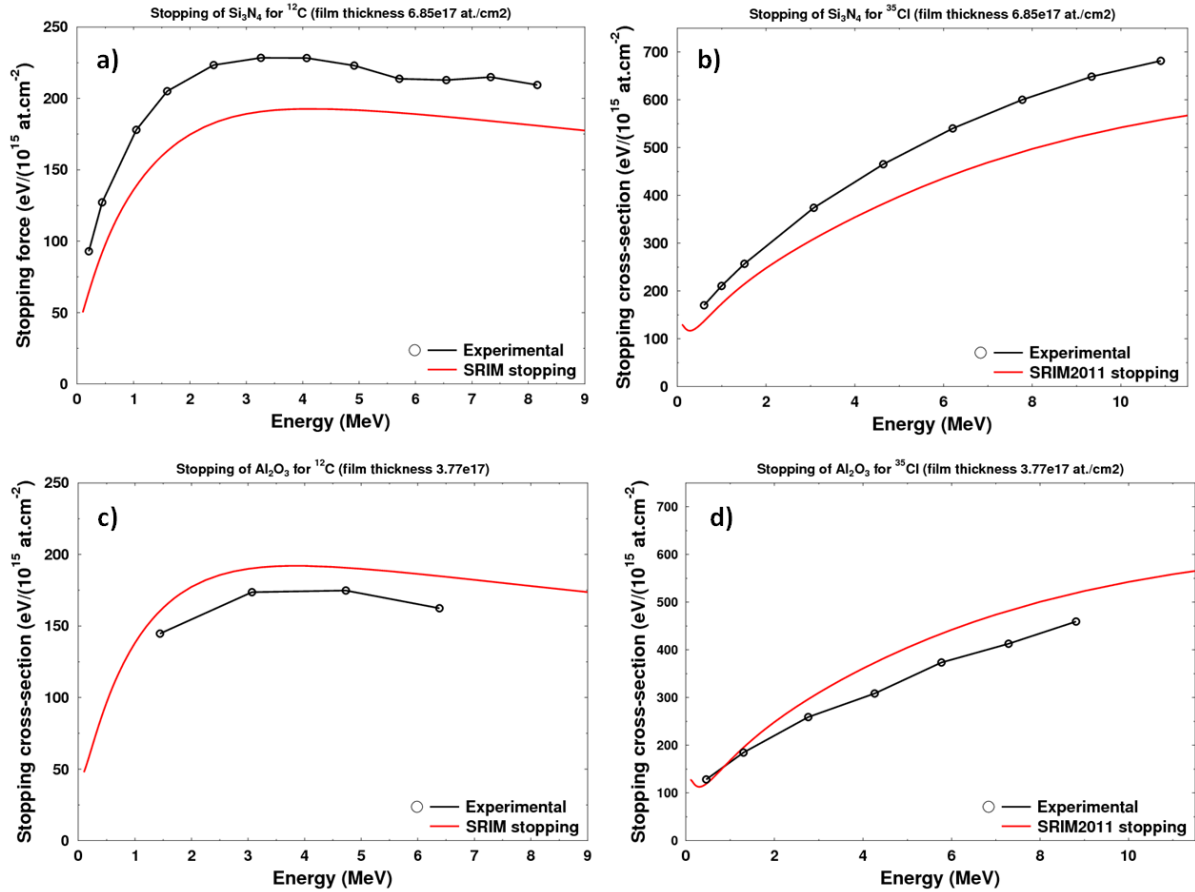
Figure 5.9: Stopping force of Si₃N₄ and Al₂O₃ for ¹²C and ³⁵Cl ions. Measured values for Si₃N₄ are higher than the SRIM. Similar deviation is measured for the Al₂O₃ with smaller stopping force values than the SRIM values.

5.3   Areal density of sub-monolayer Al₂O₃ on TiO₂

Aluminum areal densities of $5×10^{14}$ - $2×10^{15}$ at. cm^{-2} on top of 50 nm TiO$_2$ layer on a Si substrate were measured to characterize the atomic layer deposited Al$_2$O$_3$ film thicknesses in a solar cell application (see Fig. 5.10). These concentrations correspond one to five ALD cycles of Al$_2$O$_3$. This layer was used to create a barrier layer on top of the TiO$_2$ surface. While maximum of five ALD cycles was used in a deposition, the stoichiometry of the film may not be uniform and therefore this layer composition is referred only as AlO$_x$. This AlO$_x$ layer was supposed to reduce the recombination of photon created electrons in N3 dye and hence increase the efficiency of the dye sensitized solar cells. The barrier layer that formed, however, did induce a greater loss of the injected electrons through the AlO$_x$ layer and thus reduced the overall solar cell efficiency with increasing Al$_2$O$_3$ cycles. This work has been published in [V].
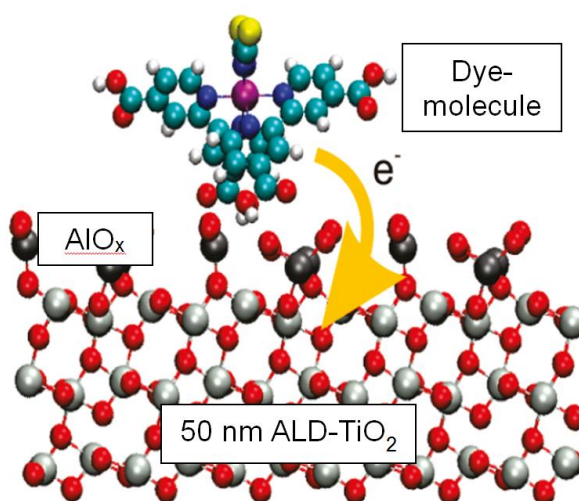
Figure 5.10: A dye molecule is attaching to the film of aluminum oxide layer on top of nanocrystalline TiO₂. Photo active N3 dye molecule electron injection through the AlOx layer was ultimately found to decrease more than the expected effect caused by the free electron recombination suppression. Reprinted (adapted) with permission from [V]. Copyright (2013) American Chemical Society, used with permission.

Concentration of aluminum atoms on TiO_2 was studied with ToF-ERDA. The 50 nm thick TiO_2 layer between the Si substrate and Al_2O_3 ALD cycles was close to ideal for the separation of the Si background from the aluminum events. Slightly thicker mid-layer would have provided close to background free aluminum events as can be seen from the ToF-E histogram in Fig. 5.11.
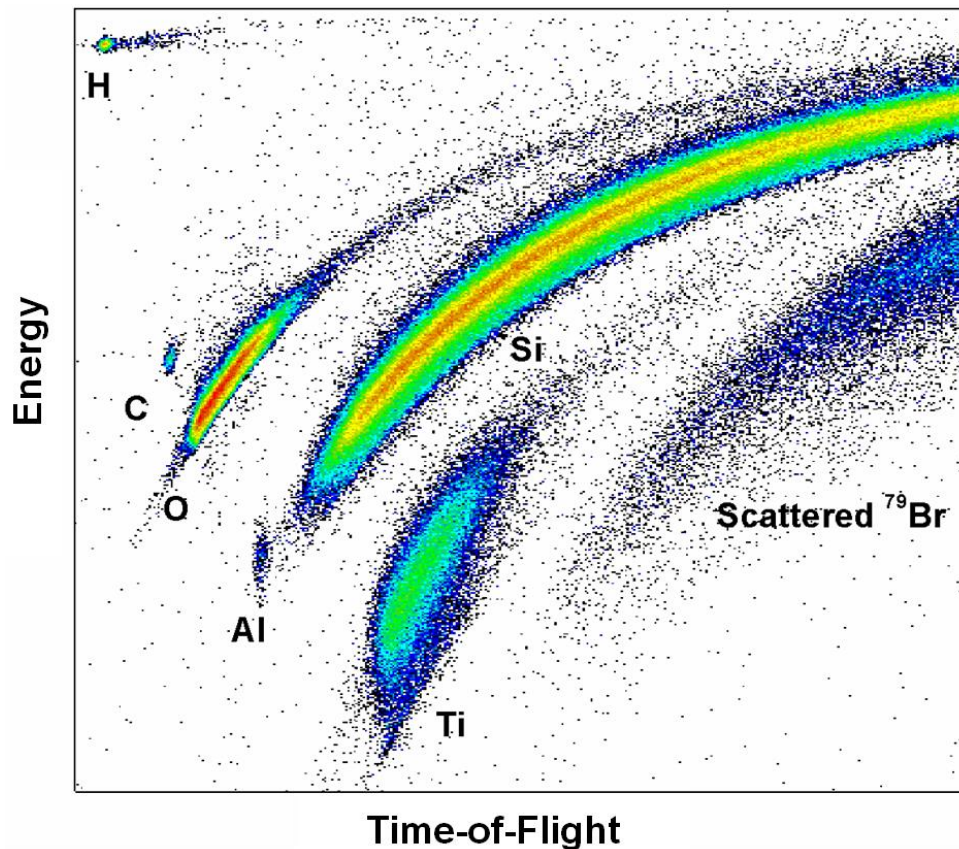
Figure 5.11: ToF-E histogram of the sample with five ALD cycles of Al_2O_3 on top of 50 nm TiO_2 on a Si substrate. The sample was measured with 8.26 MeV $^{79}Br^{4+}$. Histogram has about 370 events in the Al peak from which about 8-15 events are estimated to be due to high energy dual scattering of Si.

Total of eight samples were measured. As-deposited samples with 1, 2, 3 and 5 ALD pulses of Al_2O_3 and similar samples heat treated at 450 °C to remove excess hydrogen before the other measurements. During the analysis, the same histogram area was used in all 8 samples to determine the number of events in the Al region. The ion beam fluence was normalized to the Si substrate for all the samples and the 12 event background due to Si events was reduced from the measured Al events. This was estimated by comparing multiple same–sized areas and their measured yields between the Al main peak and the Si surface.

The results shown in Fig. 5.12 indicate a relatively linear ALD growth during the very first cycles of Al_2O_3 on top of TiO_2. Hydrogen reduction from the surface due to the heat treatment was only 10 % in average. Also, the heat treatment did not have noticeable effect to the aluminum concentrations.

These measurements proved that having low background in the ToF-ERD histogram enables sub-monolayer areal densities of elements to be probed within sufficient time and accuracy. If the mass separation is not sufficient, as could be the issue in Fig. 5.11 for Al and Si, a further separation is possible by adding an extra layer between the interfering element or mass. This was the case with this example and with TiO_2, which came naturally within the sample. Similar low concentration measurements have also been performed for boron doped

thin films of just few nanometers thick and more measurements, where growth of TiO$_2$ on top of Al$_2$O$_3$, and vice versa, will be studied in the future.
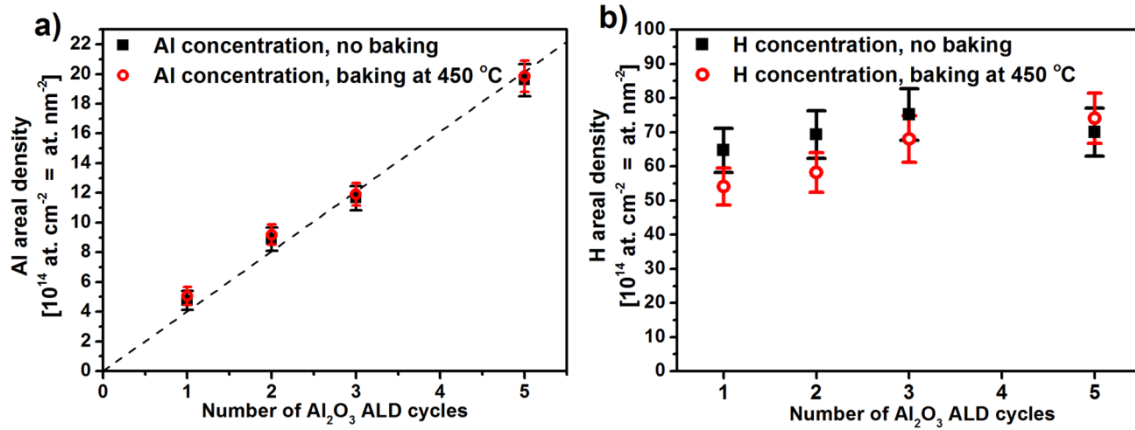

Figure 5.12: Aluminum (a) and hydrogen (b) areal density as a function of the number of ALD cycles of Al$_2$O$_3$ on TiO$_2$. Straight line in a) is a linear fit to the data with fixed zero crossing.

6   SUMMARY

Versatile tool combining time-of-flight and energy measurements in coincidence has been built for the ion beam analysis purposes and numerous ToF-ERD measurements have been performed with the tool since 2009. The carbon foil time pick-up detectors have performed reliably during these years and they have enabled depth resolutions down to 1 nm at the surface in analysis of elemental depth profiles. Their timing resolution reaches close to 150 ps and the detection efficiency for hydrogen is 40–80 % for the most typical energy range used in the ToF-ERD measurements in Jyväskylä.

An individual timing gate has been studied in detailed analyses with the help of simulations. These simulations revealed that the halo visible in many results and publications around the hydrogen isobar is due to the secondary electron effects in the individual timing gate. The halo is formed from the events in which the secondary electron emitted from the carbon foil hits the non-active area of the MCP and emits a new secondary electron which after a short flight creates a delayed event by ending to an active MCP pore.

Other simulations focused to the tandem effect which limits the resolution of this type of transmission timing detectors with biased carbon foils at low ion energies. After simulating different timing gate orientations and voltages it was concluded that T1 carbon foil dominates the tandem effect for foil voltages above 1000 V. Nearly linear dependence of the T1 foil voltage and width of the charge state distribution applies over a large T1 foil voltage range and ion mass and energy range of ions.

Analysis examples from a wide range of subjects show the applicability of the ToF-ERD tool. In typical quantitative elemental analysis of thin films as well as quantitative concentration measurements of ~0.5×10^{15} at. cm^{-2} of Al, the background suppression is essential. The time-stamped data acquisition has had a clear impact for achieving this. Work towards fully digitizing data acquisition as well as full utilization of gas ionization chamber as an energy detector will help bringing down the background even more while the energy and the depth resolution of the ToF-ERD tool will continue to improve even further.

REFERENCES

[1] The Wikipedia, *http://en.wikipedia.org/wiki/Elemental_analysis* (25.9.2013).

[2] F. Busch, W. Pfeffer, B. Kohlmeyer, D. Schüll, F. Pühlhoffer, Nucl. Instr. and Meth., 171 (1980), p. 71.

[3] M.H. Mendenhall and R.A. Weller, Nucl. Instr. and Meth. B, 59 (1991), p. 120.

[4] Z. Siketić, I.B. Radović, M. Jakšić, Nucl. Instr. and Meth. B, 266 (2008), p. 1328.

[5] K. Arstila, T. Sajavaara, J. Keinonen, Nucl. Instr. and Meth. B, 174 (2001), p. 163.

[6] M. Döbeli, R. Ender, V. Liechtenstein, D. Vetterli, Nucl. Instr. and Meth. B, 142 (1998), p. 417.

[7] V. Miikkulainen, O. Nilsen, M. Laitinen, T. Sajavaara, H. Fjellvåg, RSC Adv., 3 (2013), p. 7537.

[8] J. L'Ecuyer, C. Brassard, C. Cardinal, J. Chabbal, L. Deschenes, J. Labrie, B. Terreault, J. Martel, R.S. Jacques, J. Appl. Phys., 47 (1976), p. 381.

[9] J. Thomas, M. Fallavier, D. Ramdane, N. Chevarier, A. Chevarier, Nucl. Instr. and Meth., 218 (1983), p. 125.

[10] W. Stein and R. Leachman, Rev. Sci. Instrum., 27 (1956), p. 1049.

[11] R. Betts, Nucl. Instr. and Meth., 162 (1979), p. 531.

[12] A. Zebelman, W. Meyer, K. Halbach, A. Poskanzer, R. Sextro, G. Gabor, D. Landis, Nucl. Instr. and Meth., 141 (1977), p. 439.

[13] F.S. Goulding and B.G. Harvey, Annu. Rev. Nucl. Sci., 25 (1975), p. 167.

[14] R. Groleau, S. Gujrathi, J. Martin, Nucl. Instr. and Meth., 218 (1983), p. 11.

[15] H.J. Whitlow, G. Possnert, C.S. Petersson, Nucl. Instr. and Meth. B, 27 (1987), p. 448.

[16] S. Giangrandi, T. Sajavaara, B. Brijs, K. Arstila, A. Vantomme, W. Vandervorst, Nucl. Instr. and Meth. B, 266 (2008), p. 5144.

[17] M. Putkonen, T. Aaltonen, M. Alnes, T. Sajavaara, O. Nilsen, H. Fjellvåg, J. Mater. Chem., 19 (2009), p. 8767.

[18] M. Döbeli, C. Kottler, M. Stocker, S. Weinmann, H. Synal, M. Grajcar, M. Suter, Nucl. Instr. and Meth. B, 219 (2004), p. 415.

[19] W. Bohne, J. Röhrich, G. Röschert, Nucl. Instr. and Meth. B, 136 (1998), p. 633.

[20] Z. Siketic, I.B. Radovic, M. Jaksic, N. Skukan, Rev. Sci. Instrum., 81 (2010), p. 033305.

[21] P. Sigmund, *Stopping of heavy ions: a theoretical approach* (Springer, 2004).

[22] J. R. Tesmer, M. A. Nastasi, J. C. Barbour, C. J. Maggiore, and J. W. Mayer, *Handbook of modern ion beam materials analysis* (Materials Research Society Pittsburgh, PA, 1995).

[23] J.F. Ziegler and J.P. Biersack, Treatise on Heavy-Ion Science, (1985), p. 93.

[24] J. Biersack and J. Ziegler, *The stopping and range of ions in solids* (Springer, 1982), p. 122.

[25] W. Chu, J.W. Mayer, M. Nicolet, Academic Press, New York, (1978), p. 257.

[26] S. Giangrandi, *Low-energy Elastic Recoil Detection and Ion Beam Analysis for quantitative elemental profiling of thin films* (KU Leuven, 2010) PhD thesis.

[27] C. Kottler, *Dünnschichtanalyse mittels Vorwärtsstreuung bei tiefer Energie* (ETH Zürich, 2005) PhD thesis.

[28] P. Pusa, *Applications of theory and experiments to elastic scattering in ion beam analysis* (Helsingin yliopisto, 2004) PhD thesis.

[29] T. Sajavaara, *Heavy ion recoil spectroscopy of surface layers* (University of Helsinki, 2002) PhD thesis.

[30] H. Bethe, Annalen der Physik, 397 (1930), p. 325.

[31] F. Bloch, Z.für Physik, 81 (1933), p. 363.

[32] F. Bloch, Ann.Phys, 16 (1933), p. 287.

[33] N. Bohr, *The penetration of atomic particles through matter* (Munksgaard Copenhagen, 1948).

[34] J. S. Lilley, *Nuclear physics: principles and applications* (Wiley-VCH, 2001) 1, p. 412.

[35] S. Giangrandi, K. Arstila, B. Brijs, T. Sajavaara, A. Vantomme, W. Vandervorst, Nucl. Instr. and Meth. B, 261 (2007), p. 512.

[36] J. L'Ecuyer, J. Davies, N. Matsunami, Nucl. Instr. and Meth., 160 (1979), p. 337.

[37] H. Andersen, F. Besenbacher, P. Loftager, W. Möller, Phys. Rev. A, 21 (1980), p. 1891.

[38] J. F. Ziegler, SRIM-2008.04, www.srim.org, 2008.

[39] B. Brijs, T. Sajavaara, S. Giangrandi, K. Arstila, A. Vantomme, W. Vandervorst, Microelectron. Eng., 80 (2005), p. 106.

[40] Potku - A ToF-ERD analysis software, University of Jyväskylä, https://www.jyu.fi/fysiikka/en/research/accelerator/potku, 2013.

[41] H.J. Whitlow, H. Timmers, R.G. Elliman, T.D. Weijers, Y. Zhang, D.J. O'Connor, Nucl. Instr. and Meth. B, 195 (2002), p. 133.

[42] Y. Zhang, B.D. Milbrath, W.J. Weber, M. Elfman, H.J. Whitlow, Appl. Phys. Lett., 91 (2007), p. 094105.

[43] S. Giangrandi, B. Brijs, T. Sajavaara, K. Arstila, A. Vantomme, W. Vandervorst, Nucl. Instr. and Meth. B, 261 (2007), p. 529.

[44] Tectra, *Microchannel Plates and Microchannel Plate Detectors*, http://www.tectra.de/MCP.htm (25.2.1013).

[45] C.G. Drexler and R.D. DuBois, Phys. Rev. A, 53 (1996), p. 1630.

[46] Luma-metal, *Gold Plated Tungsten Wire*, http://www.luma-metall.se/products/gold-plated-tungsten-wire (25.2.2013).

[47] R.L. Puurunen, J. Appl. Phys., 97 (2005), p. 121301.

[48] C. Kottler, M. Döbeli, F. Glaus, M. Suter, Nucl. Instr. and Meth. B, 248 (2006), p. 155.

[49] Simion 8.1, SIMION® Ion and Electron Optics Simulator, Scientific Instrument Services, Inc.

[50] V. Baglin, I. Collins, O. Gröbner, B. Henrist, N. Hilleret, and G. Vorlaufer, in *Proc. Int. Workshop on Two-Stream Instabilities in Particle Accelerators and Storage Rings, KEK*, (2001).

[51] B. Henrist, N. Hilleret, M. Jimenez, C. Scheuerlein, M. Taborelli, and G. Vorlaufer, in *proceedings of ECLOUD, Geneva, 15-18 April 2002* (CERN Report CERN-2002-001, 2002), p. 75.

[52] F. Bordoni, Nucl. Instr. and Meth., 97 (1971), p. 405.

[53] F. Grüner, F. Bell, W. Assmann, M. Schubert, Phys. Rev. Lett., 93 (2004), p. 213201.

[54] J. Armstrong, J. Mullendore, W. Harris, J. Marion, P. Phys. Soc., 86 (1965), p. 1283.

[55] N. Novikov and Y. Teplova, in *Journal of Physics: Conference Series* (IOP Publishing, 2009), p. 082032.

[56] P.L. Smith and W. Whaling, Phys. Rev., 188 (1969), p. 36.

[57] P. Hvelplund, E. Laegsgaard, J. Olsen, E. Pedersen, Nucl. Instr. and Meth., 90 (1970), p. 315.

[58] E.J. Knystautas and M. Jomphe, Phys. Rev. A, 23 (1981), p. 679.

[59] K. Shima, T. Ishihara, T. Miyoshi, T. Mikumo, Phys. Rev. A, 28 (1983), p. 2162.

[60] K. Kukli, M. Kemell, E. Puukilainen, J. Aarik, A. Aidla, T. Sajavaara, M. Laitinen, M. Tallarida, J. Sundqvist, M. Ritala, M. Leskelä, J. Electrochem. Soc., 158 (2011), p. D158.

[61] M. Bosund, T. Sajavaara, M. Laitinen, T. Huhtio, M. Putkonen, V. Airaksinen, H. Lipsanen, Appl. Surf. Sci., 257 (2011), p. 7827.

[62] J. Hämäläinen, T. Hatanpää, E. Puukilainen, T. Sajavaara, M. Ritala, M. Leskelä, J. Mater. Chem., 21 (2011), p. 16488.

[63] J. Malm, E. Sahramo, J. Perälä, T. Sajavaara, M. Karppinen, Thin Solid Films, 519 (2011), p. 5319.

[64] M. Kariniemi, J. Niinistö, T. Hatanpää, M. Kemell, T. Sajavaara, M. Ritala, M. Leskelä, Chem. Mater., 23 (2011), p. 2901.

[65] T.J. Knisley, T.C. Ariyasena, T. Sajavaara, M.J. Saly, C.H. Winter, Chem. Mater., 23 (2011), p. 4417.

[66] J. Hämäläinen, T. Sajavaara, E. Puukilainen, M. Ritala, M. Leskelä, Chem. Mater., 24 (2011), p. 55.

[67] R.L. Puurunen, T. Sajavaara, E. Santala, V. Miikkulainen, T. Saukkonen, M. Laitinen, M. Leskelä, J. Nanosci. Technol., 11 (2011), p. 8101.

[68] L.J. Antila, M. J. Heikkilä, V. Mäkinen, N. Humalamäki, M. Laitinen, V. Linko, P. Jalkanen, J. Toppari, V. Aumanen, M. Kemell, P. Myllyperkiö, K. Honkala, H. Häkkinen, M. Leskelä, J.E.I. Korppi-Tommola, J. Phys. Chem. C, 115 (2011), p. 16720.

[69] M. Mayer, SIMNRA user's guide, Max-Planck-Inst. für Plasmaphysik, Garching, Germany, 1997.

[70] J. Jokinen, Nucl. Instr. and Meth. B, 124 (1997), p. 447.

[71] J.F. Ziegler, M. Ziegler, J. Biersack, Nucl. Instr. and Meth. B, 268 (2010), p. 1818.